An ATR-FTIR Study of Semiconductor-Semiconductor and Semiconductor-Dielectric Interfaces in Model Organic Electronic Devices

A DISSERTATION
SUBMITTED TO THE FACULTY OF THE GRADUATE SCHOOL
OF THE UNIVERSITY OF MINNESOTA
BY

TRAVIS MILLS

IN PARTIAL FULFILLMENT OF THE REQUIREMENTS
FOR THE DEGREE OF
DOCTOR OF PHILOSOPHY

XIAOYANG ZHU, ADVISOR

AUGUST 2009

Acknowledgements

My advisor, Xiaoyang Zhu has been a motivator and teacher throughout my graduate career. His expertise and creativity have helped me develop as a scientist. I owe him many thanks for his efforts and guidance. I also would like to thank every member of the Zhu research group that I have had the pleasure to work with over the last five years. I can honestly say that each person has helped me develop both scientifically and personally, and I have become good friends with many group members. I owe thanks to the University of Minnesota Department of Chemistry for its financial support, including the I. M. Kolthoff Fellowship award in 2004 and 2005.

I could never have achieved all that I have without the constant and unquestioning support of my family. Most specifically my parents, Jeff and Kathy Mills, deserve the most credit for allowing me to pursue my dreams and giving me all they could to provide for my future. My wife, Kristy, has been a constant source of inspiration and motivation for my entire graduate career. Without her I would never have made it this far. I thank her for keeping me going every day.

Abstract

Organic electronics offer many benefits to inorganic electronics such as the promise of cheap, large-scale processing on flexible substrates and incorporation into many household devices. Organic photovoltaic (OPV) devices and organic field effect transistors (OFETs) offer low-cost implementation which might compete in some applications with their inorganic counterparts. However, fundamental work is necessary to uncover the physics governing the operation of OPVs and OFETs, in order to improve the efficiency of the devices. Much of the fundamental understanding developed in this work occurs at buried interfaces, such as the donor acceptor interface in OPVs or the semiconductor dielectric interface in OFETs.

This thesis first introduces the reader to the device physics and state of the art in the development of OPVs and OFETs. After describing the experimental techniques used, a discussion of interfacial electric fields in bulk heterojunction polymer/small molecular solar cells will follow. It was found using the vibrational Stark effect, that donor acceptor interfacial electric fields could be measured and related to previous experiments. The interfacial field hinders the dissociation of excitons but also prevents geminate pair recombination. In OFET devices, the semiconductor dielectric interface was studied and the rate limiting steps to device performance in polymer electrolyte gated OFETs were determined. The interfaces studied provide insight into the fundamental operation of both OPVs and OFETs, which should help produce more efficient and controllable production of organic electronic devices.

Table of Contents

Acknowledgements i

Abstract ii

Table of Contents iii

List of Figures vi

List of Tables viii

Chapter 1. Introduction

1.1 Motivation 1

1.2 Organic semiconductors

1.2.1 Introduction 4

1.2.2 Charge transport in organic semiconductors 6

1.2.3 Charge transfer at organic-metal and organic-organic interfaces 11

1.3 Organic solar cells

1.3.1 Introduction 14

1.3.2 Materials for organic solar cell devices 15

1.3.3 Organic solar cell architectures 16

1.3.4 Bulk heterojunction solar cells 18

1.3.5 Improving efficiency in bulk heterojunction solar cell devices 20

1.4 Organic field effect transistors

1.4.1 Introduction 21

1.4.2 Dielectric materials 23

1.4.3 Polymer electrolyte dielectrics 24

1.4.4 Electrochemical and electrostatic doping mechanisms 26

1.5 References 36

Chapter 2. Instrumental Methods

2.1 Fourier transform infrared (FTIR) spectroscopy

2.1.1 Introduction 41

2.1.2 Attenuated total internal reflection FTIR (ATR-FTIR) 44

2.1.3 Vibrational Stark effect spectroscopy 46

2.2 Atomic force microscopy (AFM) 47

2.3 Profilometry and ellipsometry 48

2.4 References 54

Chapter 3. Electric fields at donor acceptor interfaces in PCBM/polymer bulk heterojunction solar cells and bilayer solar cell devices

3.1 Introduction 55

3.2 Experimental 57

3.3 Results and Discussion

3.3.1 Vibrational Stark shift in model BHJ devices 60

3.3.2 Annealing decreases interfacial electric field 61

3.3.3 Relation of film morphology to the interfacial electric field... 67

3.3.4 Model bilayer OPVs made from small molecules 67

3.4 Conclusions 70

3.5 References 85

Chapter 4. Polaron and ion diffusion in a poly(3-hexylthiophene) thin film transistor gated with polymer electrolyte dielectric

4.1 Introduction 89

4.2 Experimental 92

4.3 Results and Discussion

4.3.1 Quantitative determination of hole concentration in gate-doped P3HT 94

4.3.2 Polaron or counter ion drift/diffusion can be rate-limiting 96

4.3.3 Polarization of the polymer electrolyte is fast 101

4.4 Conclusions 102

4.5 References 107

Chapter 5. Complete Bibliography

5.1 Chapter 1 References 109

5.2 Chapter 2 References 113

5.3 Chapter 3 References 113

5.4 Chapter 4 References 117

List of Figures

Fig. 1.1 Multiple trap and release model schematic 28

Fig. 1.2 Exciton formation schematic 29

Fig. 1.3 Steps in the operation of an OPV device 30

Fig. 1.4 Chemical structures of molecules PCBM and P3HT 31

Fig. 1.5 Energy level offset between PCBM and P3HT 32

Fig. 1.6 Cartoon cross section of a BHJ blend 33

Fig. 1.7 Schematic of an OFET device 34

Fig. 1.8 Cartoon illustrating electrochemical versus electrostatic doping for polymer electrolyte gated OFET 35

Fig. 2.1 Interferometer schematic 50

Fig. 2.2 Snell's law schematic 51

Fig. 2.3 ATR-FTIR setup 52

Fig. 2.4 Illustration of the vibrational Stark effect 53

Fig. 3.1 Schematic diagram illustrating vacuum level shift for C_{60} – P3HT 72

Fig. 3.2 Geometry of model OPV device and PCBM carbonyl stretch 73

Fig. 3.3 Structures of donor polymers and vibrational Stark shifts of BHJ blends 74

Fig. 3.4 Charge transfer FTIR spectrum 75

Fig. 3.5 Vibrational Stark shift for P3HT/PCBM blends with annealing time 76

Fig. 3.6 Annealed P3HT/MEH-PPV and P3HT/PFB blends 77

Fig. 3.7 Schematic of donor – acceptor interface energetics 78

Fig. 3.8 AFM images and morphology cartoons for P3HT/PCBM blends 79

Fig. 3.9 Structure of PTCDA 80

Fig. 3.10 The four carbonyl stretches of PTCDA 81

Fig. 3.11 Illustration of bilayer sample structure 82

Fig. 3.12 Symmetric carbonyl stretches of PTCDA/small molecule bilayers 83

Fig. 4.1 Upper: Schematic of P3HT/polymer dielectric OTFT. Lower: FTIR spectrum of P3HT 104

Fig. 4.2 Upper: Gate current of model OTFT device. Lower: Total injected charge into semiconductor layer 105

Fig. 4.3 Polaron concentration as a function of time 106

Fig. 4.4 Simulated interfacial perchlorate ion concentration 107

List of Tables

Table 3.1 Frequency shifts of the PTCDA C=O stretch with respect to neutral 84

Chapter 1. Introduction

1.1 Motivation

Transistors and solar cells have been the subjects of research since Bell scientists first introduced the transistor in 1947. The discovery of conducting polymers[1-3] subsequently led to the broad field of organic electronics. That field has specific advantages over inorganic electronics, as it fulfills the desire to build electronic devices more cheaply and incorporate the devices into various new applications. One of the most promising aspects of organic electronics is the fact that the devices are built from the ground up and can therefore be made on flexible substrates. This means that devices such as transistors can be incorporated into clothing and credit cards because there is need for neither a rigid substrate nor an inorganic semiconductor such as silicon. Large scale processing of organic electronic devices is important and has been a driving force behind the organic electronics movement. Large scale processing allows for cheap mass production of devices. This is a major advantage in the photovoltaic industry, as high costs of production and installation of inorganic solar cells hinder the adoption of this technology.

What is hindering the field of organic electronics is performance. Transistors and solar cells based on traditional materials and manufacturing methods are currently more robust and more efficient. Not only is the efficiency better, the switching speeds of inorganic transistors are on the order of nanoseconds and devices operate at lower gate voltages. Another disadvantage is that because the

inorganic devices are rigid, they are easy to encapsulate and more robust. The crystalline structure of organic semiconductors is very closely related to their electronic properties. For this reason, it is very important to study and understand the structure – property relationship in organic electronic devices.

Part of this work involves understanding the mechanisms for efficiency losses in organic photovoltaics (OPVs). This is one of the most important and fundamental aspects of the field that must be understood to achieve viable devices. This is an inherently difficult problem to study and the wide range of OPV device types means there is much work remaining before the problem is understood. Bulk heterojunction (BHJ) solar cells are the most commonly studied class of OPVs. When considering efficiency-loss mechanisms for this type of organic solar cell, there are four major steps to consider between absorption of a photon of light and collection of an electron. Each step itself must be carefully studied to understand the overall fundamental device physics. Section 1.2.1 of Chapter 1 will describe the current understanding of BHJ OPV device physics in detail. Chapter 3 of this thesis is entirely devoted to understanding a single step in the operation of BHJ OPV devices: the charge transfer step.

Because the important physics to understand occur at buried interfaces within the device, attenuated total internal reflection Fourier transform infrared (ATR-FTIR) spectroscopy has been a major tool for this work. This technique and its advantages for studying this type of problem will be discussed in Chapter 2. It is useful to compare spectroscopic measurements with morphological measurements to obtain a more complete understanding of the fundamental device physics. Atomic

force microscopy (AFM) was used in this regard and will also be discussed in Chapter 2. Other techniques such as scanning electron microscopy (SEM) and transmission electron microscopy (TEM) are extremely useful and where the studies have been published in peer-reviewed literature, references to these measurements will be made as well.

Understanding the limits of organic field effect transistor (OFET) device performance is another fundamental aspect of knowledge that is extremely important to the advancement of the field of organic electronics. Chapter 4 of this work specifically examines the semiconductor-dielectric interface in order to understand what limits switching-speed of the devices and what fundamental processes occur at the interface. Further in this introduction (Section 1.4), the device physics of OFETs will be discussed as well as the importance of understanding the semiconductor-dielectric interface. Because of the buried nature of the interface, ATR-FTIR is again the primary tool used to study this problem. The difficulty in studying a buried interface lies in distinguishing any bulk experimental data from the important interfacial data. Also, it is often the case that the signal to noise levels for the data at the buried interface are low. Again, significant technical detail will be provided in Chapter 2.

Because of the use of ATR-FTIR, it is convenient to build model OFETs and OPVs on top of ATR waveguides (typically silicon and germanium crystals). The devices can be operative as a practical device, or simply a representation of the interesting layers of the device. For example, working OFETs were built on silicon waveguides and were scaled up in order to increase signal to noise ratios for FTIR

experiments. For the case of OPV devices, only the donor and acceptor materials were included in the experiments. Details regarding device fabrication will be provided in Chapter 2, with more specific experimental details also provided in Sections 3.2 and 4.2.

The intent of this thesis is to provide understanding of fundamental physics at both semiconductor-semiconductor and semiconductor-dielectric interfaces. This new understanding presented herein is applicable to the performance of both BHJ OPV and OFET devices. It also provides fundamental understanding of the chemistry and physics at the interfaces in general, which will prove useful in the future design of organic devices.

1.2 Organic Semiconductors

1.2.1 *Introduction*

Semiconductors are materials characterized by their ability to both be insulators and conductors. A semiconductor's density of states (DOS) is not continuous, but rather there is a region where electronic states are forbidden, known as the energy gap. Electrons in the semiconducting material are only allowed to have an energy in certain regions, or bands, which are in between the energy of a tightly bound electron and a totally free electron. The bands are the result of discrete quantum states of the electrons. For a semiconductor, the lower energy states are filled (bonding orbitals) and referred to as the valance band. The conduction band is empty and is the result of the anti-bonding orbitals. The energy gap between the valance and conduction bands is therefore commonly referred to as the band gap.

Since the valance band of a semiconductor is full or very nearly full, in order for an electron to move it must be excited into the conduction band from the valance band. The amount of energy required for this transition is given by the band gap of the semiconductor. The electron which is promoted to the conduction band leaves behind a vacancy, or hole, which can also be thought of as a charge carrier as the hole is free to move within the valance band.

Semiconductors are often doped with impurity atoms in order to introduce charge carriers into either the valance or conduction bands. N-type doping introduces impurity states near the conduction band of the semiconductor. The impurity atoms are oxidized by accepting holes and donating electrons to the conduction band. For example, in the case of silicon, phosphorous is commonly used as an n-type dopant, as it donates electrons to the conduction band of silicon. A dopant which is an electron acceptor, such as boron, will accept electrons from the valance band of silicon and allow conduction of holes in the valance band. This type of doping is p-type. The electrical conductivity of the resulting doped semiconductor depends on both the number of impurity atoms and the type of dopant atoms.

In contrast to inorganic semiconductors where the lattice is highly covalent and crystalline, organic semiconductors form bands through overlap of π orbitals. Therefore, the interaction between neighboring molecules is much weaker for the organic semiconductor case. The valance band is the result of overlap between the highest occupied molecular orbitals (HOMOs) and the conduction band is the result of overlap between the lowest unoccupied molecular orbitals (LUMOs) from the isolated molecule. The HOMO and LUMO states can also be thought of as the

bonding and anti-bonding orbitals. The simplest example of an organic semiconductor is polyacetylene, which is a polymer with alternating single and double bonds along its backbone. The π overlap across the backbone allows for conduction of holes when doped with iodine.[4,5] This work was the foundation for the 2000 Nobel Prize in Chemistry for the discovery of conductive polymers. Like inorganic semiconductors, organic semiconductors can be doped, but this is often unnecessary in organic electronic devices as charges are induced in several different ways besides impurity doping. This will be discussed for both organic photovoltaic devices and organic field effect transistors in the following sections.

Because of the weaker interaction between neighboring molecules in organic versus crystalline inorganic semiconductors, the mechanisms of charge transport in both amorphous inorganic semiconductors and organic semiconductors are complicated. The theories of charge transport in organic semiconductors are discussed in the following section (1.2.2).

1.2.2 *Charge transport in organic semiconductors*

Because charge transport in organic semiconductors occurs through the overlap of π orbitals, the transport depends greatly on the degree of crystallinity of the organic film. Vacuum deposited organic small molecules may be well ordered enough to be described by the multiple trap and release (MTR) model (described on page 8), as the valance or conduction bands may act as suitable transport levels. In less ordered amorphous organic semiconductors, the carriers are more localized and transport occurs by hopping between localized states. Charge hopping refers to

quantum mechanical tunneling between two localized states. Because transport by hopping depends upon overlap of quantum mechanical wavefunctions, the conductance (G) between two sites (i and j) can be described by Eq. 1.1:

$$G_{ij} = G_0 e^{-s_{ij}}.^{[6]} \tag{1.1}$$

The exponent s_{ij} is given by Eq. 1.2 and includes the tunneling process as the first term on the right hand side of the equation with an overlap parameter between the two sites (α) and the distance (R_{ij}):

$$s_{ij} = 2\alpha R_{ij} + \frac{\left|\varepsilon_i - \varepsilon_F\right| + \left|\varepsilon_j - \varepsilon_F\right| + \left|\varepsilon_i - \varepsilon_j\right|}{2k_B T}.^{[6]} \tag{1.2}$$

The second term on the right hand side in Eq. 1.2 includes the activation energy required for an upward hop in energy and the probabilities of occupation for sites i and j. The fact that this model includes both activation energy and distance means that a charge carrier can either hop a short distance with high activation energy or a long distance with low activation energy. This is known as variable range hopping (VRH).[6] The VRH model assumes a density of states ($g(\varepsilon)$) that is exponential and given in Eq. 1.3:

$$g(\varepsilon) = \frac{N_t}{k_B T_0} \exp\left(\frac{\varepsilon}{k_B T_0}\right). \tag{1.3}$$

The multiple trapping and release (MTR) model is currently used to describe charge transport in a-Si and has been used to describe charge transport in highly conjugated organic semiconductors as well.[47] In this model, delocalized states form a conduction band and valance band, both of which are associated with localized states acting as traps.[47] This is shown schematically in Fig. 1.1. In the case of p-doped pentacene, a hole traveling through the delocalized states of the valance band has potential to interact with the localized states and become trapped. Two assumptions are made in this model. The first is that a carrier arriving at a localized state will be trapped instantly. The hole can be excited out of the localized state if given enough energy. Indeed, the second assumption asserts that room temperature provides enough thermal energy to free the carrier. The mobility can now be related to mobility of the charge carrier in the delocalized band by the following:

$$\mu_D = \mu_0 \alpha e^{-\frac{E_t}{kT}}, \tag{1.4}$$

where μ_D is the drift mobility (the mobility after trapping and release), μ_0 is the charge mobility in the delocalized band, α is the ratio of density of states (DOS) at the band edge to trap states and E_t is the energy difference between trap energy and band edge.[47] It is clear that from Eq. 1.4 that mobility in a disordered film will be exponentially dependent on the depth of the trap and the temperature. While at room temperature, holes (electrons) can be excited back into the valance (conduction) band by thermal energy, but charge carrier mobility is significantly decreased because of

the presence of traps. The MTR model also predicts an effective mobility given by Eq. 1.5, where the effective mobility μ_{eff} is the free carrier mobility μ_0 times the ratio of free holes N_{free} to induced holes N_{tot}:

$$\mu_{eff}(V_G, T) = \mu_0 \frac{N_{free}}{N_{tot}}. \tag{1.5}$$

The effective mobility depends on both temperature and gate voltage (V_G). Higher gate voltages allow the lower lying traps to fill which decreases the effective activation energy for the movement of a trapped charge.

Mobility in spin-coated P3HT OFET devices is best characterized by the VHR model. For the experiments working with charge carriers in model OEFT devices in this thesis, to quantitatively describe the movement of holes through P3HT a drift/diffusion model is required because no voltage was applied to source or drain with the model devices. The solution to the one dimensional diffusion problem with two boundaries is known and given by Eq. 1.6:

$$Q(t) = C - \frac{2C}{\pi} \sum_{n=1}^{\infty} \left(\left(\frac{2}{(2n-1)^2 \pi} \right) \exp\left(-(2n-1)^2 \pi^2 \frac{Dt}{l^2} \right) \right).^{[7]} \tag{1.6}$$

In Eq. 1.6, C is saturation concentration at $t \to \infty$, D is the diffusion constant, and l is the channel length. In the experiments with model OFET devices, charge carriers were induced into the channel by an applied gate voltage.

In order to produce charge carriers in un-doped organic semiconductors and without applying a gate voltage (such as in the case of OPVs), external energy is required to promote an electron from the valance band to the conduction band. When organic semiconductors are excited by an external source of energy such as light, an electron in the valance band is excited into a higher energy level, leaving behind a hole. Whether or not the electron and hole are free or Coulombically bound to one another in a semiconductor with hydrogen-like wavefunctions depends on the Bohr radius of the lowest electronic state, given by Eq. 1.7:

$$r_B = r_0 \varepsilon \left(\frac{m_e}{m_{eff}} \right) \tag{1.7}$$

and the critical distance between the two charges (Eq. 1.8):

$$r_c = \left(\frac{q^2}{4\pi\varepsilon\varepsilon_0 k_B T} \right). \tag{1.8}$$

[8]

In Eq. 1.7, m_e is the mass of a free electron in vacuum, m_{eff} is the effective mass of an electron in the semiconductor, r_0 is the Bohr radius for a ground state hydrogen atom (0.53 Å) and ε is the dielectric constant. In Eq. 1.8, q is the fundamental charge, ε_o is the permittivity of free space, k_B is Boltzmann's constant and T is the temperature. The electron and hole are Coulombically bound to each other if $r_c > r_b$. This condition is known as an exciton, and the pair is treated as a single neutral particle.

The absorption of energy to form an exciton in a semiconductor is illustrated schematically in Fig. 1.2.

The electron and hole will recombine if they do not separate within the excitonic lifetime. The singlet exciton lifetime for model electron acceptor C_{60} has been determined through time-resolved photoluminescence experiments to be 0.3 ns.[9] Within this time, the exciton was also found to diffuse 28 nm, a quantity referred to as the exciton diffusion length.[9] The lifetime and diffusion length of an exciton are important quantities for OPV materials, as they determine certain design rules for organic solar cells which will be discussed in section 1.3.3.

1.2.3 *Charge transfer at organic-metal and organic-organic interfaces*

The fundamental physics governing OPV device operation depend greatly on the energetics at the donor acceptor interface. Chapter 3 will explain in detail the effects of morphology on interfacial energetics and device performance. This section is meant to serve as an introduction to and review of recent work in the field of charge transfer at organic-metal and organic-organic interfaces.

To begin to understand charge transfer between two organic molecules, an understanding of charge transfer between a metal substrate and an organic molecule is the best place to begin. The simplest hypothesis of how an organic metal interface works is called the Schottky-Mott limit, which assumes vacuum level alignment between the metal and semiconductor. It was once thought that even though vacuum level alignment had been disproved for inorganic semiconductor semiconductor interfaces, for organic-metal interfaces vacuum level alignment was acceptable

because the interaction between organic and metal is not significant.[10] This was proven to be false by numerous studies on various metal organic interfaces which show the breakdown of the vacuum level alignment rule.[10] This means that one cannot use the properties of isolated molecules to determine interfacial energetics. Much more complex theories revealed a better understanding of the physics at metal organic interfaces. Such theories involve charge transfer at the interface, so that a dipole becomes present between the two materials. The dipole strength can be easily measured using photoelectron spectroscopy[10-12] but the nature of the charge transfer has been the topic of some debate.

There has been no widely accepted universal picture describing interfacial charge transfer, but several theories have been proposed. Interactions between metals and organic molecules are usually classified by Van der Walls physisorption or covalent-like chemisorption.[13] Within this framework, the interaction has been described using the interface density of states model (which was originally proposed for inorganic semiconductor metal interfaces and later adopted for metal organic interactions).[14-16] Vázquez et al. calculated an induced density of interface states in the organic semiconductor energy gap which was high enough to control interfacial dipole formation.[17] A charge neutrality level for the organic molecule was then proposed which can be determined for different organic semiconductors and then applied to different systems such as organic – organic interfaces.[17] The charge neutrality level is the result of a broadened molecular density of states due to molecule metal interaction. Its position is determined such that the total integrated density of states accommodates the number of electrons in the isolated molecule.[18]

Once determined for a molecule, the position of the charge neutrality level can be used to predict charge transfer between two organic molecules with known charge neutrality levels. For example, Vázquez, Kahn, et al. used their measured charge neutrality levels for several organic molecules and predicted interfacial dipoles compared to the values measured with photoelectron spectroscopy with a high degree of accuracy.[18,19] The theory predicts that negative charge is transferred between organic molecules from lower to higher charge neutrality level. This results in a decrease in the initial offset between charge neutrality levels and the formation of an interfacial dipole. The amount of charge transfer is predicted by a screening parameter, which is a function of the dielectric constants of the two materials.

A similar suggestion has also been proposed to explain the formation of the interfacial dipole.[20-22,28] It is similar in that both mechanisms involve charge transfer between interface states. However, the ideas are very different in the assumed interaction strengths at the interfaces. Integer charge transfer assumes Van der Walls type bonding and electronic coupling via tunneling.[28] Therefore, a much stronger interaction between the two organic semiconductors is assumed. Photoelectron studies by Osikowicz et al. have shown similar results for the interfacial dipole between C_{60} and P3HT, with the negative pole of the dipole residing on the C_{60} phase.[28] However, the authors argue that an interfacial dipole of 0.6 eV cannot be accounted for with doping or impurity induced space charge, because the levels or impurity theoretically required for this are unrealistically high. The authors argue that charge will spontaneously transfer from donor to acceptor until equilibrium is reached. For example, in the P3HT/C_{60} system, electronic states

in the P3HT are depopulated (forming polaronic P^+ states), transferring charge into negative charge transfer states (CT^-) on the C_{60}. This spontaneous charge transfer occurs until an equilibrium between P^+ polaronic states and CT^- states is reached. Essentially, energy is gained as charge is transferred from P3HT to C_{60} at the interface. If conditions for spontaneous charge transfer are not met (i.e. the P^+ energy level of a polymer falls above the CT^- states of the C_{60}), then additional energy is required to form a dipole and spontaneous charge transfer will not occur. This was shown to be the case for the poly(9,9-di-*n*-octylfluorenyl-2,7-diyl) (F8)/C_{60} system. In Chapter 3, the mechanisms for formation of the interfacial dipole will be revisited.

1.3 Organic Solar Cells

1.3.1 *Introduction*

The function of a solar cell is to convert energy in the form of photons into electric current which can do work in an external circuit. To accomplish this, a semiconducting material is required. The photon transfers its energy to an electron which is moved into an excited state. An exciton must separate into a free electron and hole by moving to an energetically favorable state. This can be accomplished by placing two semiconductors in direct contact with one another to form an interface. At the interface, ideal conditions elicit the lowest unoccupied molecular orbitals (LUMOs) of the two semiconductors offset by an energy slightly larger than the exciton binding energy. This allows for downhill flow of charge carriers as they move into separate phases. To achieve such energetic offset, intrinsic n and p-type

organic semiconductors are used to form the junction. N-type organic semiconductors act as electron acceptors and p-type act as electron donors. In an OPV device, n-type and p-type organic semiconductor materials are placed together and photon absorption and exciton formation occur in the donor and acceptor phases, and charge separation occurs at the interface. Charge collection results after the separated charges move through their transport phases (electrons in the n-type material and holes in the p-type) to electrodes. Schematically, these steps are shown in Fig. 1.3.

1.3.2 *Materials for organic solar cell devices*

The ideal n and p-type organic semiconductors for use in photovoltaic applications need to have an optimal energy gap between highest occupied molecular orbital (HOMO) and lowest unoccupied molecular orbital (LUMO) for absorption of energy in the solar spectrum. The portion the of solar spectrum which is absorbed by each material is wavelengths between 350 nm and an upper wavelength defined by the band gap of the material.[23] Most organic semiconductors studied have bandgaps between 1.8 and 5.0 eV.[24] The materials working in tandem that have produced the highest efficiency bulk heterojunction (BHJ; this architecture will be discussed in sections 1.3.3 and 1.3.4) organic solar cells to date are poly(3-hexylthiophene) (P3HT) and [6,6]-phenyl-C_{61} butyric acid methyl ester (PCBM).[25-27] The two molecules are shown in Fig. 1.4. P3HT in its regioregular form produces very ordered structures and possesses a high degree of crystallinity. Also, a vacuum-level offset between the molecules is estimated to be 0.6 eV based on the offset between

P3HT and C_{60}.[28] This energy drop is sufficient to separate electron hole pairs, whose exciton binding energy has been measured to be 0.4 – 0.5 eV.[29] Fig. 1.5 illustrates the energy offset between PCBM and P3HT schematically.

PCBM and C_{60} are small molecule acceptors that are often used in conjunction with other donor polymers. Poly(9,9′-dioctylfluorene-co-bis-*N*,*N*′-(4-butylphenyl)-bis-*N*,*N*′-phenyl-1,4-phenyldiamine) (PFB) and poly(2-methoxy-5-(2'-ethyl-hexyloxy)-1,4-phenylene vinylene) (MEH-PPV) are commonly used donor polymers and their effects on OPV efficiency when blended with PCBM will be discussed in Chapter 3. The molecular weight of the donor polymer is an additional consideration, and the effect of the molecular weight of P3HT on P3HT/PCBM blends will also be discussed in Chapter 3.

OPV devices can also be made with vacuum-deposited small molecules. The efficacy of the two small molecules working together as an OPV depends on the relative energy-level offset and the amount of interfacial electric field induced. The interfacial electric field at vacuum-deposited small molecule interfaces will be examined in Chapter 3 as well. The common small molecule semiconductors investigated in this work include 3,4,9,10-perylenetetracarboxylic dianhydride (PTCDA), copper phthalocyanine (CuPc), 4,4'-N,N'-dicarbazolyl-biphenyl (CBP), *N*, *N* ′-bis-(1-naphthyl)-*N*,*N* ′-diphenyl1-1,1-biphenyl1-4,4′-diamine (α-NPD), bathocuproine (BCP) and tris-(8-hydroxyquinoline) aluminum (Alq_3).

1.3.3 *Organic solar cell architectures*

In order to achieve maximum efficiency in OPV devices, certain design rules

must be considered. The most efficient dissociation of exciton into free charge carriers occurs at the donor acceptor interface.[30,31] This the area of this interface must therefore be maximized while still considering the efficacy of light absorption of the photovoltaic materials. This means maximizing the donor acceptor interface while optimizing the thicknesses of each layer to allow for maximum light absorption. This optimization requires that any exciton created in either the donor or acceptor must diffuse to the nearest interface before recombining. Given the exciton diffusion length measured for P3HT/PCBM devices,[9] the optimum thickness of each layer is about 60 nm. This optimum thickness takes into account the fact that once a free electron and hole have been generated, they must move to the anode and cathode (respectively) of the device in order to be collected and used in the circuit. A charge carrier that either spends too much time in its transport phase or has too far of a distance to travel before collection will recombine with its counterpart.

In keeping with these design rules, there are several types of OPV architectures which are in use in current devices. The simplest is a multilayer device whose structure is a layer of donor material and a layer of acceptor material sandwiched between metal electrodes. The problem with this architecture is that the layers need to be on the order of 100 nm thick, and with an exciton diffusion length on the order of 10 nm (28 nm in C_{60}),[9] some excitons are being generated but not converted into free carriers. A way to increase film thickness for optimal light absorption while minimizing the length the excitons must diffuse is to mix the donor and acceptor layers together between two electrodes. This architecture is called the bulk heterojunction (BHJ) and is the primary solar cell architecture used in this research.

BHJ solar cell devices are typically made by blending donor polymer with acceptor small molecule. Efficiency is highly improved with the BHJ solar cells over the multilayer cells and processing is straightforward as well. However, the result of uncontrolled blending donor and acceptor will yield a device which has isolated phases and layers that are too thick or thin in each phase.[32] Fig. 1.6 is a cartoon representation of a cross section of a typical BHJ blend. Donor and acceptor phases which are isolated islands will be able to separate excitons into free charge carriers, but the carriers will be marooned on the islands and never collected, decreasing efficiency. Because of the importance of the BHJ solar cell to this thesis work, BHJ devices will be discussed in greater detail in the following section (1.3.4). To reduce the island effect, controlled-growth BHJ solar cells are currently being investigated.[32] This involves creating continuous carrier conducting pathways using organic vapor phase deposition. Yang et al. showed that substrate temperature, chamber pressure, and high molecular surface diffusivity are critical factors which can be optimized for growth of ordered blends with high surface areas and continuous pathways.[32] Further improvements to OPVs that go beyond the manipulation of device architecture are discussed in section 1.3.5.

1.3.4 *Bulk heterojunction solar cells*

The basic operation and structure of the BHJ solar cell were presented in the previous section. As mentioned, this architecture is the primary solar cell device type examined in this thesis research. This section will provide more detail on the BHJ solar cell and the current understanding of efficiency-loss mechanisms in these

devices.

The bulk of the work performed recently on bulk heterojunction solar cells has involved devices made by mixing small molecule electron acceptors with conjugated polymer donors.[30,31,33,34] The most commonly studied materials are PCBM (acceptor molecule) and regio regular P3HT (donor polymer).[26,27,35] Upon mixing, the result is a spontaneous phase separation of the polymer and small molecule which forms nano-scale charge-separating heterojunctions throughout the bulk of the material.[30,36] The active layer is sandwiched between two electrodes: one transparent and one reflecting. Indium tin oxide (ITO) is the usual choice for the transparent conductive electrode.

Efficiency-loss mechanisms in the BHJ solar cell are not well understood. It has been shown that only 61% of electron hole pairs dissociate into free carriers under short circuit conditions (i.e. no external circuit).[37] Other mechanisms such as bimolecular recombination result in the loss of free charge carriers and are not well understood.[38,39] It was described in section 1.2.3 that charge will transfer at the interface between two organic semiconductors creating an interfacial dipole and resulting electric field. Understanding this interfacial field is critical to the understanding of electron hole pair separation and efficiency loss mechanisms in BHJ OPVs.

A vacuum level shift of 0.6 eV with respect to P3HT has been measured at the P3HT C_{60} interface.[28] This number will be adopted for the vacuum-level offset between P3HT and PCBM, as the two systems are very similar. This energy-level offset is the result of charge transfer between the donor and acceptor and as a result,

an interfacial dipole is formed pointing from donor to acceptor (positive to negative). Arkhipov et al. suggested this dipole makes exciton dissociation more efficient by preventing geminate pair recombination at the donor-acceptor interface.[40] It has also been suggested that the main cause of efficiency loss in excitonic solar cells is geminate pair recombination.[41] The binding energy of such geminate electron hole pairs across the interface has been reported to be approximately 0.3 eV.[42] Intuitively however, one would expect the electric field associated with the dipole to hinder the dissociation of an exciton due to electrostatic repulsion encountered by the hole and electron in the donor and acceptor materials respectively. These ideas raise an important question: what role does the interfacial electric field play in exciton dissociation and the overall quantum efficiency? This question will be addressed in detail in Chapter 3.

1.3.5 *Improving efficiency in bulk heterojunction solar cell devices*

This section will review research in the field of BHJ photovoltaics aimed at improving the efficiency of organic solar cells in general. BHJ solar cells are inherently excitonic, which means there are several key steps where efficiency must be maximized. When the steps are broken down into their individual efficiencies, the result is Eq. 1.9, which is the definition of external quantum efficiency (η_{EQE}).[43]

$$\eta_{EQE} = \eta_A \eta_{IQE} = \eta_A \eta_{ED} \eta_{CT} \eta_{CC} \tag{1.9}$$

η_A is the efficiency of photon absorption leading to exciton generation and the

internal quantum efficiency (η_{IQE}) is defined as the ratio of charge carriers collected to the number of photons absorbed; it is the product of the efficiencies of exciton diffusion, charge transfer and charge carrier collection, respectively. The charge transfer step is the dissociation of an exciton into free charge carriers, where the attractive Coulombic potential between electron and hole must be overcome. To best improve efficiency, a balance must be struck between increasing the amount of photons absorbed by decreasing the polymer bandgap and minimizing energy loss at the charge transfer step. Calculations have predicted that 10% efficiency is achievable with an optimal polymer bandgap of 1.4 eV.[44] Contrasting calculations have shown that the ideal bandgap for the polymer is 1.9 eV and the maximum power conversion efficiency should be at least 10.8%.[45] The difference is the result of the latter calculation placing more emphasis on the charge transfer step. This is ideal for the improvement of P3HT/fullerene systems because the bandgap of P3HT is 1.9 eV.[46] Much emphasis has been placed on engineering polymers with lower bandgaps[46] but efficiency can be optimized using P3HT systems by focusing on the charge transfer step.[45] Understanding the interfacial electric field will prove critical to understanding the performance of BHJ OPV devices.

1.4 Organic Field Effect Transistors

1.4.1 *Introduction*

Chapter 4 deals with the fundamental physics and rate-limiting steps involved in the operation of organic field effect transistors (OFETs) gated with a polymer electrolyte dielectric. This section will provide an introduction to the operation of

OFET devices and the physics governing their operation.

The organic field effect transistor facilitates the transport of charge between a source and drain electrode through an active channel made of organic semiconductor material. A third electrode, the gate electrode, is separated from the active channel by an insulating dielectric material and facilitates the amount of charge carriers available to transport charge in the channel. When a bias is applied to the gate electrode, charge carriers are swept into the organic semiconductor and provide a path for flow of current. With no bias on the gate, there should be no charge carriers in the channel and no current (known as off current) between the source and drain electrodes. The OFET is shown schematically in Fig. 1.7.

There are benchmarks used to compare the performance of OFETs to inorganic thin film transistors (TFTs). The usual benchmark material is amorphous silicon (a-Si) and properties include on to off current ratio (I_{on}/I_{off}), charge carrier mobility (μ) in the accumulation regime and operating gate voltages (V_G).[47,48] In order for OFETs to compete with the a-Si TFTs currently used in liquid crystal displays (LCDs), for example, on to off current ratio would have to be 10^6 or higher, charge carrier mobility at least 1 $cm^2\ V^{-1}\ s^{-1}$ and operating voltages need to be reduced to only a few volts. In many cases, operating voltages for OFETs exceed 10 V out of the necessity to induce a high number of charge carriers. The reason that a higher gate voltage induces more carriers is due to the production of a higher electric field. The gate voltage is directly proportional to the charge accumulated per unit area by Eq. 1.10, where V_G is the gate voltage and C_i is the capacitance of the dielectric per unit area:[49]

$$\frac{\text{Charge}}{\text{Area}} = V_G C_i. \tag{1.10}$$

These higher voltages need to be applied to the gate in order for OFETs to operate properly. This establishes a major problem: mainly the fact that high operating voltages have been required to achieve reasonable mobility. One avenue that is pursued in an attempt to achieve these goals is utilizing a novel polymer electrolyte dielectric between gate electrode and organic layer in the OFET.[33,56-58] This technique has been successful as operating voltages are significantly lowered. However, an in-depth understanding of the limiting factors in device performance is necessary and will be discussed in detail in Chapter 4.

1.4.2 *Dielectric materials*

The main components of the OFET which dictate its performance are the organic semiconductor and the dielectric material. As discussed in the previous paragraph, the choice of dielectric plays an influential role in the performance of the OFET. In order for an OFET to operate, charge must build up on each side of the dielectric material as explained in the previous section. Dielectrics therefore are insulators and the higher the capacitance of the dielectric material, the lower the voltage required to induce charges in the OFET. Traditional dielectric materials are semiconductor oxides, which naturally form on the surface of an inorganic semiconductor in atmosphere. For silicon, the SiO_2 layer can be grown at high

temperatures in a controlled manner and forms an excellent semiconductor-dielectric interface.

For the case of OFET devices, the dielectric material is just as important as with inorganic transistors, but harder to build because of the flexibility requirement. Nanodielectrics, which consist of several layers of highly polarizable molecules have been proposed and shown promise.[50-52] These layers allow "mobile" charges to travel up and down the molecular wire structures and thus polarize the dielectric medium. Ion-gel dielectrics have gained much attention recently as well.[53] These consist of an ionic liquid and block copolymer matrix. The high capacitance (>10 $\mu F\ cm^{-2}$) and fast switching speeds (~1 ms) make this type of dielectric very desirable. Similar to the ion-gel dielectric is the polymer electrolyte dielectric, which consists of mobile ions dissolved in a polymer matrix. Poly(ethylene oxide) : lithium perchlorate (PEO:$LiClO_4$) systems have demonstrated high capacitance in OFET devices.[56-58] Polymer electrolyte dielectrics will be discussed in detail in section 1.4.3.

1.4.3 *Polymer electrolyte dielectrics*

In order to achieve the best performance for OFET devices, dielectric materials consisting of mobile ions dissolved in a polymer electrolyte matrix[54] are being actively developed.[55-59] This is because the effective capacitance of such dielectric layers is 10 $\mu F\ cm^{-2}$, which is 10^3 times larger than that of conventional dielectrics such as semiconductor oxide. The capacitance (C) is directly related to the charge density (Q) and inversely related to the applied voltage (V) by the following equation

(Eq. 1.11):

$$C = \frac{Q}{V}. \tag{1.11}$$

Therefore, the advantage of having the high capacitance is that the gate voltage which operates the device can be much lower than with conventional dielectric materials. For OFET devices which incorporate polymer electrolyte dielectrics, fundamental physical questions are raised such as what steps limit how fast the device can turn on and off and what is the mechanism for charge injection into the semiconductor layer. The mobility of charge carriers in the semiconductor phase (μ) is related to the charge carrier density by Eq. 1.12:

$$\mu = \left(\frac{L}{W}\right)\frac{I_D}{QV_D}, \tag{1.12}$$

where L and W are the channel length and width respectively and I_D and V_D are the current and voltage between source and drain respectively.[30] A question of interest when considering the operation of OFETs gated with high-capacitance polymer electrolyte dielectrics is how fast are they able to turn on and off and what limits this performance. This will be discussed in detail in Chapter 4 using $LiClO_4$ ions inside a poly(ethylene oxide) matrix as the dielectric material. P3HT is used as the organic semiconductor. Depending on the different operating voltages, different regimes of

device operation are observed. This is best illustrated by explaining the concepts of electrochemical and electrostatic doping in polymer electrolyte gated OFETs.

1.4.4 *Electrochemical and electrostatic doping mechanisms*

Charges can be induced in the organic semiconducting layer by the polymer electrolyte dielectric by two different mechanisms. Because the ions within the polymer matrix are mobile, they are free to move not only within the matrix but also into the organic semiconductor. The degree to which the mobile ions penetrate the semiconductor-dielectric interface defines the doping mechanism. When the ions penetrate deep within the semiconductor layer, the semiconductor is electrochemically doped. Ions contained mainly at the interface dope the semiconductor electrostatically.

The distinction between electrostatic and electrochemical doping is a difficult one to quantitatively make and is somewhat meaningless anyway. The distinction does become important and less ambiguous when determining the rate-limiting steps in OFET device operation. Therefore, electrostatic doping is defined as the distinct interface between the semiconductor layer and polymer matrix, with mobile ions of one polarity accumulating in the polymer matrix and charge carriers of opposite sign accumulating on the organic semiconductor side. Electrostatic doping induces charge in only a very thin portion of the organic semiconductor immediately next to the dielectric matrix.

In contrast, electrochemical doping is the mass transfer of ions into the organic semiconductor bulk. In this case, the entire organic semiconductor sample can be

doped. There are ways to distinguish between electrostatic and electrochemical doping mechanisms. There are distinct spectroscopic signatures associated with electrochemical doping.[60,61] Additionally, the electrochemical mechanism is unambiguous at high gate voltages as the total injected charge density is well beyond what can be accommodated by a few molecular layers. In comparison, the electrostatic doping mechanism is usually believed to be operative at low gate bias. However, the point at which electrostatic doping becomes electrochemical is difficult to define. For example, the simple picture of an electrical double layer may apply for OTFTs based on organic single crystals, as the penetration of ions into the organic semiconductor is hindered by the close-packed crystal structure. However, roughness and a distribution of structural defects at the surface of a molecular or polymer film may permit the diffusion or partial penetration of ions into the first layer of the organic semiconductor phase. This process resembles the electrochemical mechanism, but only for the interface region of the organic semiconductor (not the entire film). When considering the operation of OFETs, it is most important to think about what is limiting the performance of the device. Is it the diffusion rate of the mobile ions in the electrochemical regime or the actual charge carriers in the semiconductor in the electrostatic regime? These questions will be addressed in Chapter 4.

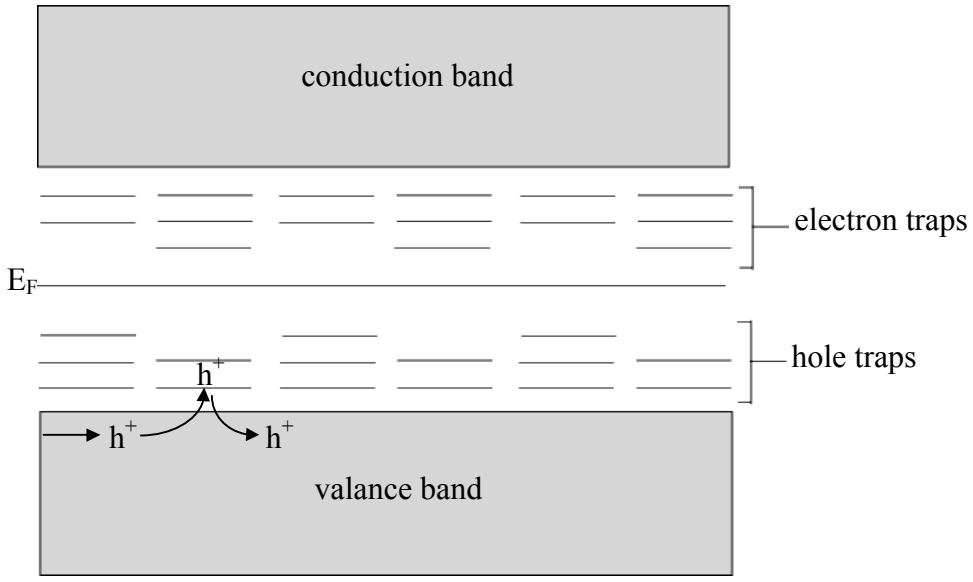

Figure 1.1 Schematic of the multiple trapping and release (MTR) model, a model for charge transport that is generally accepted for amorphous Si and crystalline organic semiconductors. A delocalized hole in the valance band can become trapped in a localized state. Thermal energy is necessary to release the hole from the delocalized state.

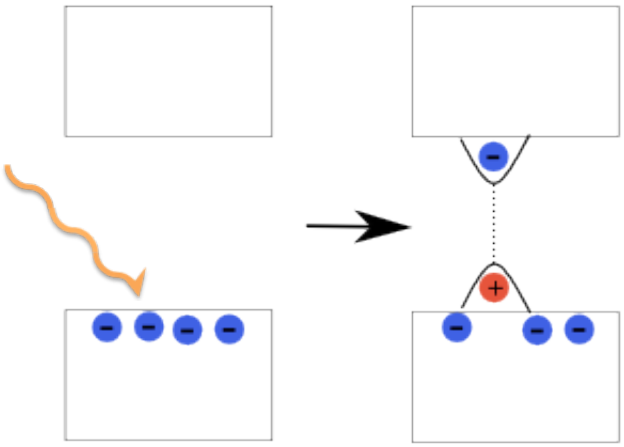

Figure 1.2 Energy absorption in an organic semiconductor leads to the formation of an exciton. After light absoption, an electron is promoted into an excited state, leaving behind a positively charged vacancy (hole). The electron and hole are Coumbically bound.

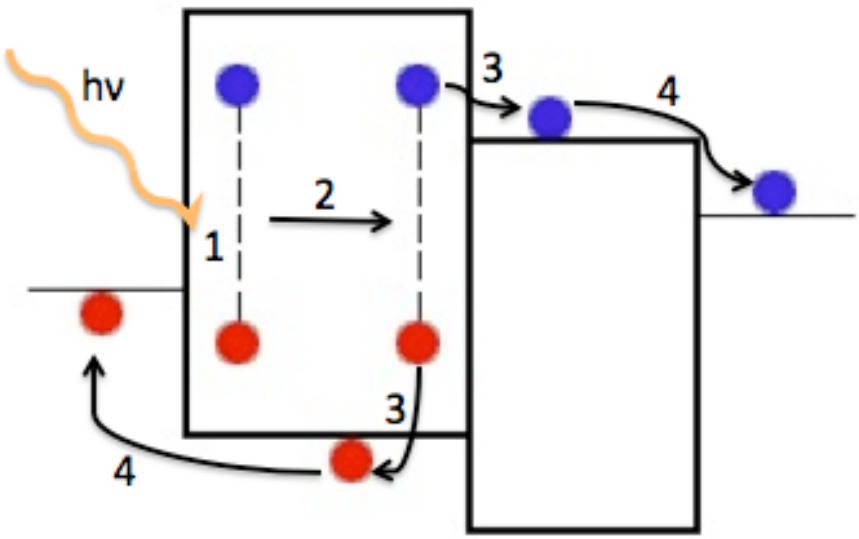

Figure 1.3 The steps involved in photogenerated charge carrier collection. Step 1 is exciton formation and step 2 is diffusion of the exciton to a donor acceptor interface. Step 3 is exciton dissociation, the splitting of an exciton into free charge carriers. This step is most efficient at the interface between donor and acceptor. Step 4 is charge transport and collection at the cathode (holes) or anode (electrons).

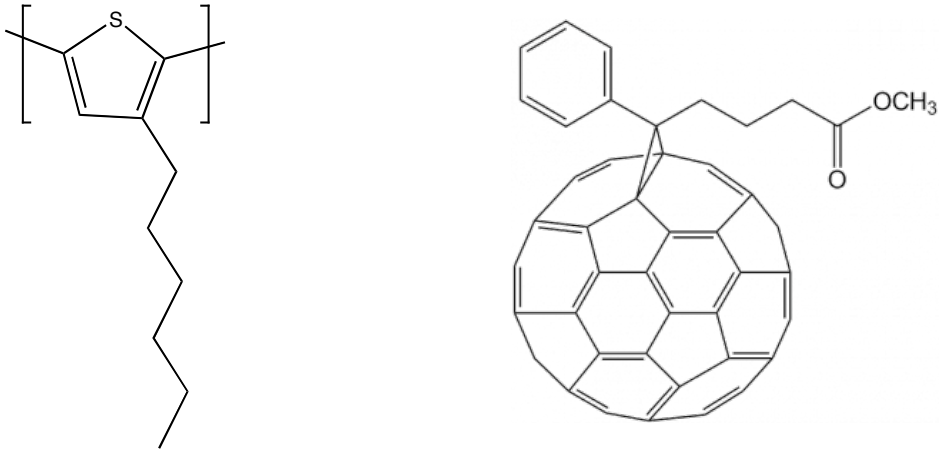

P3HT PCBM

Figure 1.4 Figure 1.4 shows the chemical structures of P3HT and PCBM.

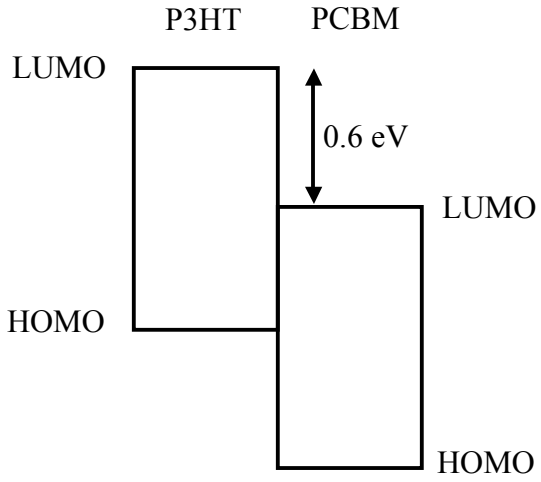

Figure 1.5 Figure 1.5 schematically illustrates the energy offset between P3HT and PCBM. The 0.6 eV offset between the LUMOs of P3HT and PCBM ensures that the separation of an exciton will be energetically favorable at the interface.

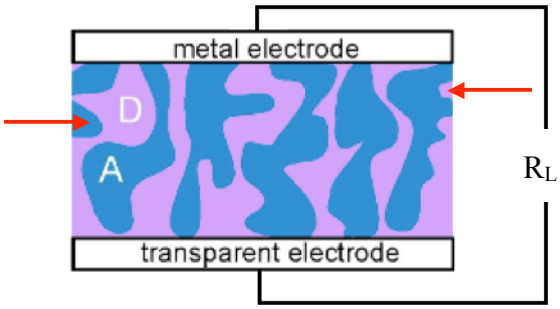

Figure 1.6 Cross section of a typical BHJ solar cell. The red arrows indicate isolated regions of donor and acceptor that cannot contribute to the overall cell efficiency.

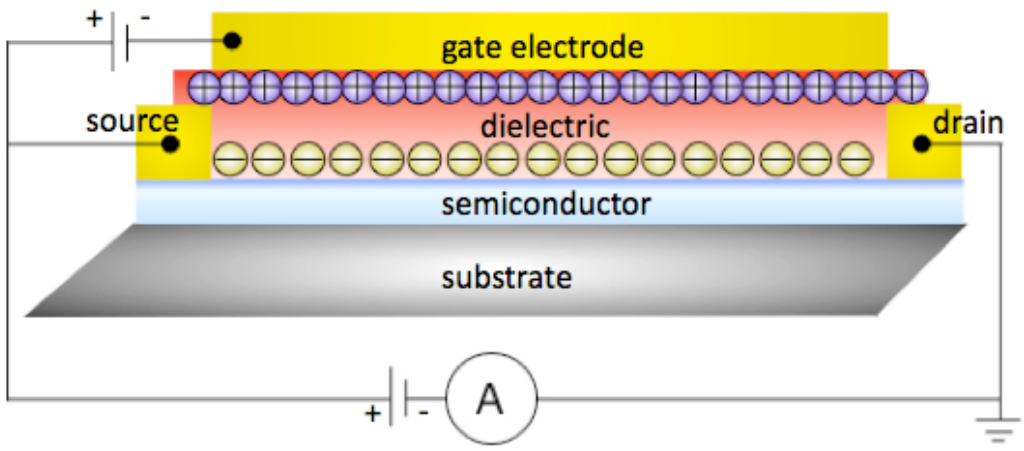

Figure 1.7 A schematic representation of an organic field effect transistor. The current from source to drain through the semiconductor is modulated by the gate voltage which induces charge carriers into the semiconductor channel. This is accomplished by using a dielectric which will polarize due to the electric field from applied gate voltage.

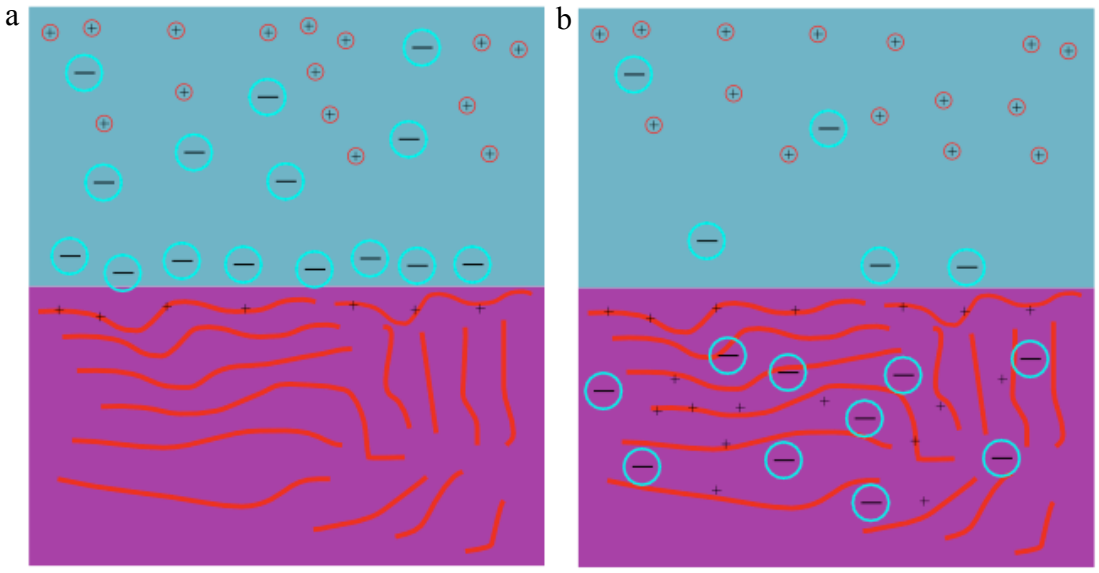

Figure 1.8 Cartoon illustrating electrochemical versus electrostatic doping for a polymer electrolyte gated OFET. The electrostatic regime is shown in panel a. The mobile ions of the dielectric material do not penetrate deeply into the semiconductor, thus charge carriers are only induced in the first few layers of semiconductor material. Panel b shows the electrochemical doping regime. Here, the mobile ions penetrate deep within the semiconductor and potentially the entire semiconductor film may become charged.

1.5 References

[1] B. A. Bolto, R. McNeill, D. E. Weiss, *Aust. J. Chem.* **1963**, 19, 1090.

[2] R. McNeill, D. E. Weiss, D. Willis *Aust. J. Chem.* **1965**, 18, 477.

[3] B. A. Bolto, D. E. Weiss, D. Willis *Aust. J. Chem.* **1965**, 18, 487.

[4] J. McGinness, P. Corry, P. Proctor *Science*, **1974**, 183, 853.

[5] H. Shirakawa, E. J. Louis, A. G. MacDiarmid, C. K. Chiang, A. J. Heeger *J. Chem. Soc. Chem. Comm.*, **1977**, 474, 578.

[6] M. C. J. M. Vissenberg, M. Matters *Phys. Rev. B* **1998**, 57, 12964.

[7] D. L. Powers *Boundary Value Problems*, 3rd Ed. **1987** (Harcourt Brace College Publishers, Fort Worth).

[8] S.-S. Sun, N. S. Sariciftci *Organic Photovoltaics: Mechanisms, Materials and Devices* **2005** (CRC Press).

[9] H. Gommans, S. Schols, A. Kadashchuk, P. Heremans, S. C. J. Meskers *J. Phys. Chem. C* **2009**, 113, 2974.

[10] A. Kahn, N. Koch, W. Gao *J. Polymer Science B: Polymer Phys.* **2003**, 41, 2529.

[11] D. Cahen, A. Kahn *Adv. Mater.* **2003**, 15, 271.

[12] W. R. Salaneck, R. H. Friend, J. L. Bredas *Phys. Rep.* **1999**, 319, 231.

[13] N. Koch *J. Phys. Condens. Matter* **2008**, 20, 184008.

[14] F. Flores, C. Tejedor *J. Phys. Chem. C* **1987**, 20, 145.

[15] W. Mönch *Surf. Sci.* **1994**, 299, 928.

[16] H. Vázquez, R. Oszwaldowski, P. Pou, J. Ortega, R. Perez, F. Flores, A. Kahn *Europhys. Lett.* **2004**, 65, 802.

[17] H. Vázquez, F. Flores, R. Oszwaldowski, J. Ortega, R. Perez, A. Kahn *Appl. Surf. Sci.* **2004**, 234, 107.

[18] H. Vázquez, W. Gao, F. Flores, A. Kahn *Phys. Rev. B* **2005**, 71, 041306.

[19] A. Kahn, W. Zhao, W. Gao, H. Vázquez, F. Flores *Chem. Phys.* **2006**, 325, 129.

[20] C. Tengstedt, W. Osikowwicz, W. R. Salaneck, I. D. Parker, Che-H. Hsu, M. Fahlman *Appl. Phys. Lett.* **2006**, 88, 053502.

[21] S. Braun, W. Osikowicz, Y. Wang, W. R. Salaneck *Org. Electron.* **2007**, 8, 14.

[22] A. Crispin, X. Crispin, M. Fahlman, M. Berggren, W. R. Salaneck *Appl. Phys. Lett.* **2006**, 89, 213503.

[23] G. Dennler, M. C. Scharber, T. Ameri, P. Denk, K. Forberich, C. Waldauf, C. J. Brabec *Adv. Mater.* **2008**, 20, 579.

[24] J. Hwang, A. Wan, A. Kahn *Mater. Science Eng. R* **2009**, 64, 1.

[25] J. Y. Kim, S. H. Kim, H.-H. Lee, K. Lee, W. Ma, X. Gong, A. J. Heeger, *Adv. Mat.* **2006**, 18, 572.

[26] G. Li, V. Shrotriya, J, Huang, Y. Yao, T. Moriarty, K. Emery, Y. Yang, *Nat. Mater.* **2005**, 4, 864.

[27] Y. Kim, S. Cook, S. M. Tuladhar, S. A. Choulis, J. Nelson, J. R. Durrant, D. D. C. Bradley, M. Giles, I. McCulloch, C.-S. Ha, M. Ree, *Nat. Mater.* **2006**, 5, 197.

[28] W. Osikowicz, M. P. de Jong, W. R. Salaneck, *Adv. Mater.* **2007**, 19, 4213.

[29] V. I. Arkipov, H. Bässler, *Phys. Status Solidi A* **2004**, 201, 1152.

[30] G. Yu, J. Gao, J. Hummelen, F. Wudl, A. J. Heeger *Science* **1995**, 270, 1789.

[31] J. J. M. Halls, C. A. Walsh, N. C. Greenham, E. A. Marseglia, R. H. Friend, S. C. Moratti, A. B. Holmes *Nature* **1995**, 376, 498.

[32] F. Yang, M. Shtein, S. R. Forrest *Nat. Mater.* **2005**, 4, 37.

[33] N. S. Sariciftci, L. Smilowitz, A. J. Heeger, F. Wudl *Science* **1992**, 258, 1474.

[34] J. Y. Kim, K. Lee, N. E. Coates, D. Moses, T.-Q. Nguyen, M. Dante, A. J. Heeger *Science* **2007**, 317, 222.

[35] W. Ma, C. Yang, X. Gong, K. Lee, A. J. Heeger *Adv. Funct. Mater.* **2005**, 15, 1617.

[36] S. H. Park, A. Roy, S. Beaupré, S. Cho, N. Coates, J. S. Moon, D. Moses, M. Leclerc, K. Lee, A. J. Heeger *Nature Photon.* **2009**, 3, 297.

[37] V. D. Mihailetchi, L. J. A. Koster, J. C. Hummelen, P. W. M. Blom, *Phys. Rev. Lett.* **2004**, 93, 216601.

[38] I. Riedel, J. Parisi, V. Dyakonov, L. Lutsen, D. Vanderzande, J. C. Hummelen *Adv. Funct. Mater.* **2004**, 14, 38.

[39] P. Schilinsky, C. Waldauf, C. J. Brabec *Appl. Phys. Lett.* **2002**, 81, 3885.

[40] V. I. Arkhipov, P. Heremans, H. Bäsler, *Appl*. *Phys*. *Lett*. **2003**, 82, 4605.

[41] R. A. Marsh, C. R. McNeill, A. Abrusci, A. R. Campbell, R. H. Friend, *Nano Lett.* **2008**, 8, 1393.

[42] H. Ohkita, S. Cook, Y. Astuti, W. Duffy, S. Tierney, W. Zhang, M. Heeney, I. McCulloch, J. Nelson, D. D. C. Bradley, J. R. Durrant, *J. Am. Chem. Soc.* **2008**, 130, 3030.

[43] P. Peumans, A. Yakimov, S. R. Forrest *J. Appl. Phys.* **2003**, 93, 3693.

[44] M. C. Scharber, D. Mühlbacher, M. Koppe, P. Denk, C. Waldauf, A. J. Heeger, and C. J. Brabec *Adv. Mater.* **2006**, 18, 789.

[45] L. J. A. Koster, V. D. Mihailetchi, P. W. M. Blom *Appl. Phys. Lett.* **2006**, 88, 093511.

[46] E. Bundgaard, F. C. Krebs *Sol. En. Mater. Sol. Cells* **2007**, 91, 954.

[47] G. Horowitz *Adv. Mater.* **1998**, 10, 365.

[48] C. D. Dimitrakapoulos, P. R. L. Malenfant *Adv. Mater.* **2002**, 14, 99.

[49] A. R. Brown, C. P. Jarrett, D. M. de Leeuw, M. Matters *Synth. Met.* **1997**, 88, 37.

[50] M.-H. Yoon, A. Facchetti, T. J. Marks *Proc. Nat. Acad. Sci.* USA **2005**, 102, 4678.

[51] S. Ju, K. Lee, D. B. Janes, M.-H. Yoon, A. Facchetti, T. J. Marks *Nano Lett.* **2005**, 5, 2281.

[52] S. Ju, D. B. Janes, G. Lu, A. Facchetti, T. J. Marks *Appl. Phys. Lett.* **2006**, 89, 193506.

[53] J. Lee, M. J. Panzer, Y. He, T. P. Lodge, C. D. Frisbie *J. Am. Chem. Soc.* **2007**, 129, 4532.

[54] F. M. Gray, *Solid Polymer Electrolytes: Fundamentals and Technological Applications* **1991** (VCH, New York).

[55] J. Takeya, K. Yamada, K. Hara, K. Shigeto, K. Tsukagoshi, S. Ikehata, Y. Aoyagi *Appl. Phys. Lett.* **2006**, 88**,** 112102.

[56] M. J. Panzer, C. D. Frisbie *Appl. Phys. Lett.* **2006**, 88, 203504.

[57] M. J.Panzer, C. R. Newman, C. D. Frisbie, *Appl. Phys. Lett.* **2005**, 86, 103503.

[58] M. J. Panzer, C. D. Frisbie, *J. Am. Chem. Soc.* **2007**, 129, 6599.

[59] A. S. Dhoot, J. D. Yuen, M. Heeney, I. McCulloch, D. Moses, A. J. Heeger, *Proc. Nat. Acad. Sci. USA* **2006**, 103, 11834.

[60] L. G. Kaake, Y. Zou, M. J. Panzer, C. D. Frisbie, X-Y. Zhu, *J. Am. Chem. Soc*. **2007**, 129, 7824.

[61] J. D. Yuen, A. S. Dhoot, E. B. Namdas, N. E. Coates, M. Heeney, I. McCulloch, D. Moses, A. J. Heeger, *J. Am. Chem. Soc.* **2007**, 129, 14367.

Chapter 2. Instrumental Methods

2.1 Fourier Transform Infrared (FTIR) Spectroscopy

2.1.1 *Introduction*

Because the primary goal of this thesis research is to better understand the limiting factors in organic electronic device performance and elucidate structure – property relationships, Fourier transform infrared spectroscopy (FTIR) is a useful tool. It is used to study model devices which are subjected to operating conditions such as applied voltage to examine structural changes to the organic molecules in the device. IR spectroscopy works by probing the vibrational frequencies of chemical bonds. The interaction of the infrared radiation with the matter provides information on the structure of the material. Two atoms bonded together will vibrate as if connected by a spring. The frequency of vibration (v) depends on the reduced mass (μ) of the atoms and force constant (k) for the bond, as shown is Eq. 2.1:

$$v = \frac{1}{2\pi}\sqrt{\frac{k}{\mu}} \tag{2.1}$$

Absorption of radiation can cause the vibration to jump to a higher frequency or an excited vibrational state. Only discrete frequencies are allowed for the bond, which are integer multiples of the ground state energy. The ground state vibrational energy is given by Eq. 2.2:

$$E = \frac{1}{2}h\nu, \tag{2.2}$$

and the higher frequency allowed vibrations by Eq. 2.3:

$$E = \left(n + \frac{1}{2}\right)h\nu. \tag{2.3}$$

The infrared radiation incident on a sample will be absorbed and the vibrational energy of the bond will move to an excited state if the energies of the transition and incident radiation match. The absorbance (A) is related to the concentration of absorbents (c) by Beer's law (Eq. 2.4):

$$A = \varepsilon bc, \tag{2.4}$$

where b is the path length the light travels through the sample and ε is the molar absorptivity parameter specific to each absorbent.

FTIR has several advantages over conventional or dispersive IR spectroscopy. Importantly, when using FTIR, all of the information at all frequencies is collected simultaneously. When looking at changes in the spectra that occur over time, this is an advantage. Additionally, a gain in the signal-to-noise ratio is achieved when using an interferometer. There is a speed advantage to collecting an interferogram and a spectrum in the same amount of time, as a factor of $\frac{1}{2}N$

more time is available for the measurement, resulting in a signal-to-noise advantage of the Fellgett factor:

$$\text{Fellgett factor} = \left(\frac{1}{2}N\right)^{1/2}.^{[1]} \tag{2.5}$$

These advantages are achieved because the IR light passes through an interferometer and then through the sample. The output signal is the interferogram, and the traditional spectrum can be generated by performing a Fourier transform on the output. The interferometer is designed to split a single coherent beam of IR light into two beams which travel different and varying lengths. The beams then recombine to form an alternating interference pattern on the detector. The interferogram shows alternating regions of constructive and destructive interference, because the two beams either travel varying distances or pass though different optical media. Whether or not the beams interfere constructively or destructively depends on the multiple of the wavelength of the light. Integer multiples result in constructive interference while half-integer multiples result in destructive interference. The schematic setup of an interferometer is shown in Fig. 2.1. The coherent beam from the source passes through a mirror which allows 50% of the light to pass through and reflects 50% at an angle. The integer wavelengths are created by holding one of the mirrors fixed and moving the other so as to create the interference pattern. The light then passes to a detector.

The detector used for study of the OPV and OFET systems was a Mercury (Hg) Cadmium (Cd) Telluride (Te) (MCT) detector. The MCT detector is a photodetector and allows for frequency detection in the mid-IR region of the electromagnetic spectrum, due to the bandgap of CdTe which is 1.5 eV. HgTe has a bandgap of nearly 0, which allows for IR detection from approximately 500 cm^{-1} to 5000 cm^{-1}. This range encompasses the vibrational frequencies encountered when studying organic semiconducting materials. C=O and C=C vibrations will be used as reporter groups and have approximate vibrational frequencies of 1740 cm^{-1} and 1610 cm^{-1} respectively.

2.1.2 *Attenuated total internal reflection FTIR (ATR-FTIR)*

The most interesting aspects to examine regarding the structure – property relationship are the buried interfaces. In OPVs, the interfaces are between the donor and acceptor while in OFETs the interface is between the semiconductor and dielectric. When examining these buried interfaces, standard vibrational spectroscopic techniques such as transmittance spectroscopy cannot be used due to the large absorbance cross section of the metal electrodes. It is necessary to employ a form of vibrational spectroscopy called attenuated total internal reflection (ATR) FTIR. This allows for the structural examination of buried interfaces with high spectral resolution. Electrodes which are necessary for simulating the operating conditions of organic electronic devices can also be incorporated into the devices without interfering with the IR signal. This technique has been successfully demonstrated by Jun et al.[2]

ATR behaves according to the law of refraction, also called Snell's law, given in Eq. 2.6:

$$n_1 \sin\theta_1 = n_2 \sin\theta_2, \tag{2.6}$$

where n_1 and n_2 refer to the indices of refraction for materials 1 and 2, and θ refers to the angle of the incident light with respect to normal. Fig. 2.2 illustrates the law of refraction. It is applied to the experiment by guiding the IR beam through a silicon or germanium waveguide at an angle of incidence θ = 45˚. Because the angle of incidence exceeds the critical angle as defined by Eq. 2.7, the beam passing through the waveguide cannot escape and is totally internally reflected.[1]

$$\sin\theta = \frac{n_2}{n_1} \tag{2.7}$$

The wave travels from a denser medium (germanium; n_1 = 4.02) to a less dense medium (organic material; $n_{2\ (polystyrene)}$ = 1.55) and is refracted further from the surface normal.[1] Thus, the IR beam is guided through the waveguide and passed to a detector. The sample on top of the waveguide is probed by an evanescent wave which is generated at each bounce within the waveguide. The physical explanation for the generation of the evanescent wave is that even though the light is totally internally reflected, the electric and magnetic fields cannot be discontinuous at the boundary between the different optical materials. As a result, an evanescent standing

optical wave propagates normal to the interface in the less dense medium and decays exponentially with distance from the interface. The schematic ATR-FTIR setup is shown in Fig. 2.3. The depth of penetration (d) of the evanescent wave can be calculated using Eq. 2.8:

$$d = \frac{\lambda}{2\pi n_1 \sqrt{\sin^2\theta - (n_2 / n_1)^2}}. \tag{2.8}$$

For example, at 1500 cm^{-1}, using the refractive indices given on page 45 and an incident angle θ = 45°, the penetration depth of the evanescent wave from the interface is approximately d = 1.1 μm.

2.1.3 *Vibrational Stark effect spectroscopy*

In order to understand changes in interfacial conditions upon mixing two materials, vibrational Stark effect spectroscopy is a valuable tool. Using this technique, electric field can be related to shifts in vibrational frequency. This type of spectroscopy has been used to study interfacial electric fields in the protein community[3,4] and was recently applied to organic – organic interfaces.[5,6] Fig. 2.4 shows the anharmonic oscillator potential energy curve along with the ground state vibrational energy and excited vibrational states. The example spectra shown are the carbonyl stretch of PCBM. With no external electric field, an absorption of energy to excite the C=O to the next highest vibrational state results in the black trace, centered about 1736.5 cm^{-1}. With applied electric field, the ground state and excited

state vibrational energy levels are shifted, but by different amounts. This is the result of Eq. 2.8:

$$H = H_0 - \mu F, \tag{2.8}$$

where H is the field-dependent Hamiltonian, H_0 is the unperturbed Hamiltonian, μ is the Stark tuning rate and F is the electric field. As a result, subsequent energy absorption will cause a blue shift in the spectrum, as illustrated by the blue trace in panel b of Fig. 2.4.

The shift in frequency ($\Delta\nu$) is related to the electric field (F) by Eq. 2.9:

$$\Delta\nu = -\Delta\mu \cdot F - \frac{1}{2} F \cdot \Delta\alpha \cdot F. \tag{2.9}$$

The factor $\Delta\mu$ is called the Stark tuning rate, which is the quantity to relate frequency shift to electric field. This number is specific to each vibration and is found in the literature for a variety of functional groups. The second order Stark tuning rate (change in dipole polarizability) is $\Delta\alpha$.

2.2 Atomic force microscopy (AFM)

The structural measurements described above are complimented with the topographic imaging technique atomic force microscopy (AFM). The scanning probe tip rasters across the sample surface and mechanical forces between the tip and

sample are converted into a topographic image. The AFM consists of a sharp tip (the radius of curvature is typically on the order of 10 nm) connected to a silicon nitride cantilever with a known spring constant (k = 10-100 N/m). When the tip is brought into close proximity to the sample surface, forces cause the tip to move and as a result the cantilever will twist. The AFM is able to measure electrostatic interactions, van der Walls forces and capillary forces. The cantilever motion is detected by bouncing laser light of the cantilever onto a four quadrant photodetector. The photodetector is able to interpret the motion of the cantilever and send the signal to the AFM software which will form a topographic image of the sample surface. An electronic feedback mechanism is employed in order to maintain a constant force between the sample and tip. The two main types of imaging modes are contact mode and tapping (non-contact) mode. Contact mode takes a measurement by sliding the tip across the surface. Tapping mode is exclusively used in this thesis work to examine soft polymer/small molecule samples. Tapping mode works by intermittently making contact with the surface and is much less destructive than contact mode because shear forces are eliminated. This is why it is usually chose to measure soft surfaces like organic materials. The cantilever is driven to oscillate near its resonant frequency and the forces between the tip and sample cause perturbation to the cantilever oscillation. The tip / cantilever are raster scanned across the surface and a topographic image is recorded.

2.3 Profilometry and ellipsometry

Profilometry is a similar to AFM in that a scanning probe is moved over a

surface and measures changes in topography. The tip used in a profilometer usually has a much large radius of curvature than the AFM tip. Therefore, spatial resolution is limited compared to the AFM, but vertical resolution can easily be determined. Profilometry was used to determine the thicknesses of spun polymer films on glass, silicon or germanium substrates by looking at the step height from bare substrate to organic material.

Ellipsometry is a non-destructive technique that is used to measure film thickness and optical properties. It measures changes in polarization of incident light upon reflection off or transmission through a sample. In this work, light was reflected off the sample surface to determine the thickness of the organic layer deposited on the waveguide.

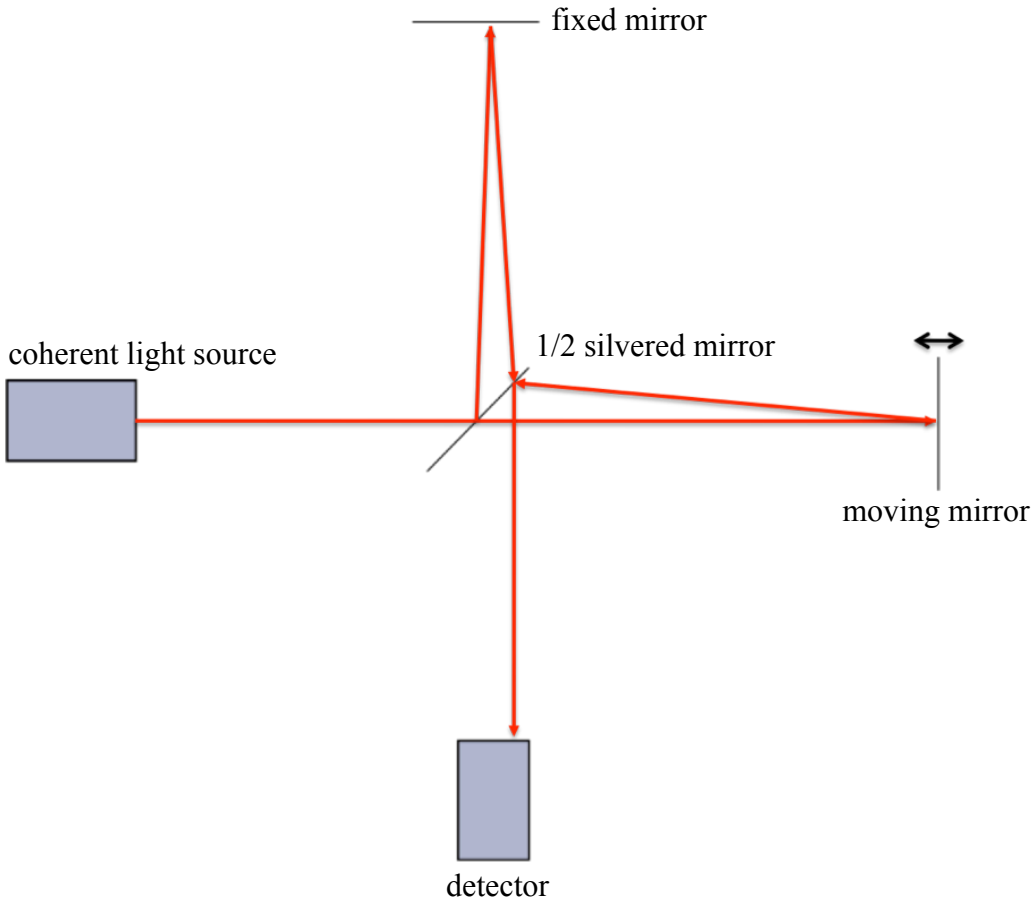

Figure 2.1 Schematic illustration of the interferometer. The interferometer is designed to split a single coherent beam of IR light into two beams which travel different and varying lengths. The beams then recombine to form alternating interference pattern on the detector. The interferogram shows alternating regions of constructive and destructive interference, because the 2 beams travel varying distances due to the moving mirror.

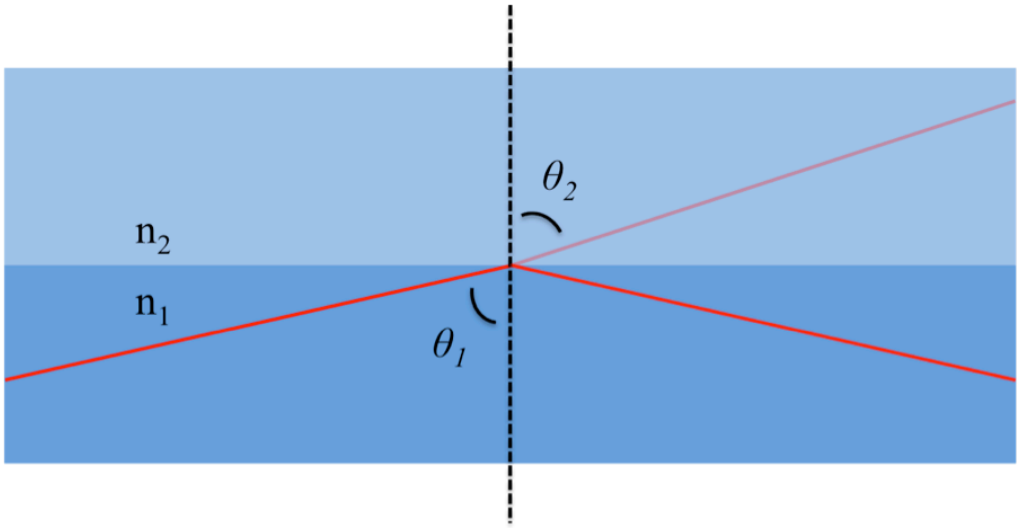

Figure 2.2 Schematic illustration of the law of refraction, also called Snell's law. n_1 and n_2 refer to the indices of refraction for materials 1 and 2, and θ refers to the angle of the incident light with respect to normal. See Figure 2.3 for an illustration showing how this law is applied to the experimental work.

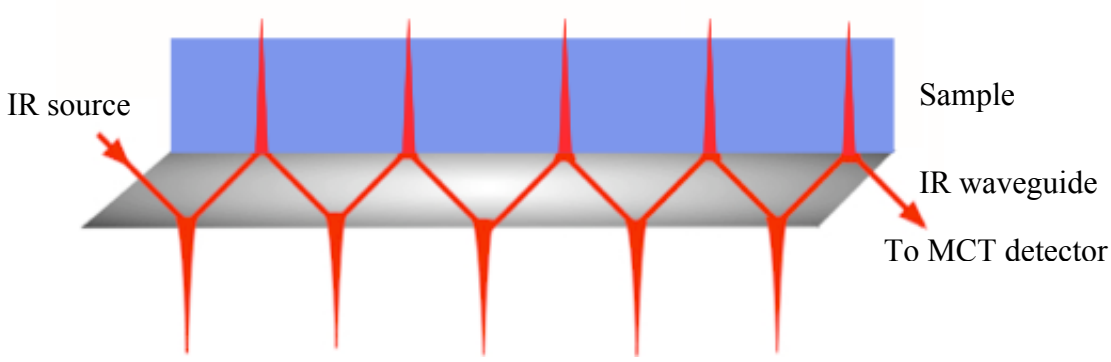

Figure 2.3 Schematic of the ATR-FTIR setup. The IR beam passing through the silicon or germanium waveguide will be totally internally reflected and an evanescent wave will form at each bounce. The evanescent wave, which is perpendicular to the interface and extends approximately 1 μm from the interface, is used to probe the sample.

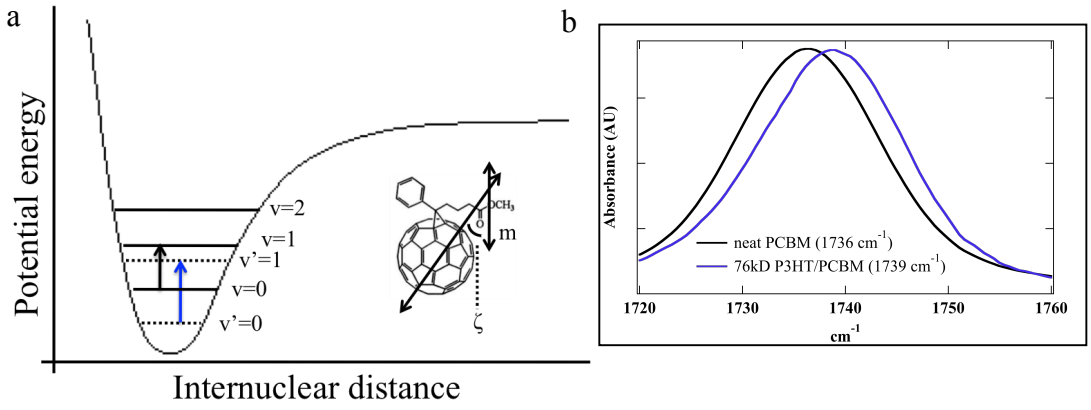

Figure 2.4 An illustration of the vibrational Stark effect. Panel a shows the anharmonic oscillator potential energy curve along with the ground state vibrational energy and excited vibrational states. The example spectra shown are the carbonyl stretch of PCBM. With no external electric field, an absorption of energy to excite the C=O to the next highest vibrational state results in the black trace, centered about 1736.5 cm^{-1}. With applied electric field, the ground state and excited state vibrational energy levels are shifted, but by different amounts. As a result, subsequent energy absorption will cause a blue shift in the spectrum, as illustrated by the blue trace in panel b. If the angle between the incident radiation (ζ) and the bond's dipole moment (m) $\neq 0$, a scaling factor must be used to determine the correct value for the electric field.

2.4 References

[1] J. E. Stewart *Infrared Spectroscopy Experimental Methods and Techniques* **1970** (Marcel Dekker Inc., New York).

[2] Y. Jun, X.-Y. Zhu *J. Am. Chem. Soc.* **2004**, 126, 13224.

[3] A. Chattopadhyay, S. G. Boxer *J. Am. Chem. Soc.* **1995**, 117, 1449.

[4] L. N. Silverman, M. E. Pitzer, P. O. Ankomah, S. G. Boxer, E. E. Fenlon *J. Phys. Chem. B Lett.* **2007**, 111, 11611.

[5] L. W. Barbour, R. D. Pensack, M. Hegadorn, S. Arzhantsev, J. B. Asbury *J. Phys. Chem. C* **2008**, 112, 3926.

[6] R. D. Pensack, K. M. Banyas, L. W. Barbour, M. Hegadorn, J. B. Asbury *Phys. Chem. Chem. Phys.* **2009**, 11, 2575.

Chapter 3. Electric fields at donor acceptor interfaces in PCBM/polymer bulk heterojunction solar cells and bilayer solar cell devices

3.1 Introduction

Bulk-heterojunction (BHJ) solar sells incorporating blends of electron donor polymers and electron accepting small molecules have the highest efficiency for organic excitonic photovoltaic devices.[1,2] While organic solar cells are inefficient compared to their inorganic counterparts, organic photovoltaics (OPVs) have potential advantages such as manufacture by roll-to-roll processing and the ability for assembly on flexible, inexpensive substrates. OPV devices are therefore promising candidates for solar energy conversion. However, the efficiency of the organic devices must improve to render the field an effective alternative to current energy solutions. BHJ solar cells are inherently excitonic, which means there are several key steps where efficiency must be maximized. When the steps are broken down into their individual efficiencies, the result is Eq. 3.1, which is the definition of external quantum efficiency (η_{EQE});

$$\eta_{EQE} = \eta_A \eta_{IQE} = \eta_A \eta_{ED} \eta_{CT} \eta_{CC} . \quad (3.1)$$

η_A is the efficiency of photon absorption leading to exciton generation, and the internal quantum efficiency (η_{IQE}) is defined as the ratio of charge carriers collected to the number of photons absorbed; it is the product of the efficiencies of exciton diffusion, charge transfer, and charge carrier collection, respectively. The charge

transfer step is the dissociation of an exciton into free charge carriers, where the attractive Coulombic potential between electron and hole must be overcome. This exciton binding energy is estimated to be on the order of 0.4 – 0.5 eV.[3] Therefore, the free energy difference between the lowest unoccupied molecular orbital (LUMO) levels of the donor and acceptor should be approximately the same magnitude as the exciton binding energy for optimal solar cell efficiency. The theoretical energy difference between LUMO levels for P3HT and PCBM is 1.0 eV, and considerable research is underway to tune the bandgaps of acceptor materials in order to achieve maximum efficiency at the charge transfer step. This work examines how morphology and interfacial energetics affect the efficiency of exciton dissociation.

Blends incorporating poly(3-hexylthiophene) (P3HT) and [6,6]-phenyl-C_{61} butyric acid methyl ester (PCBM) have been shown to make OPV devices with the highest quantum efficiencies.[4-6] Part of the reason for this is that P3HT is highly regioregular and forms a very ordered structure. When PCBM and P3HT are blended, an electron is transferred from P3HT to PCBM. A vacuum level shift of 0.6 eV with respect to P3HT has been measured at the P3HT C_{60} interface,[7] and this number will be adopted for the vacuum level offset between P3HT and PCBM. The vacuum level refers to the energy at which an electron is no longer bound to the solid; above the vacuum level an electron is free. It is used as a reference to define ionization energy and electron affinity. For a donor – acceptor blend, charge transfer dictates the interfacial energy level alignment and as a result, an offset between the vacuum levels of the two phases occurs. This energy level offset results in an

interfacial dipole pointing from donor to acceptor (positive to negative). Fig. 3.1 illustrates the vacuum level shift.

Additionally, bilayer devices made from the thermal deposition of small molecules were investigated. Work by Vázquez et al. has predicted the strength of the interfacial dipole for small molecule interfaces.[30-33] In small molecule organic solar cells as well as in BHJ solar cells, the role the interfacial electric field plays in device performance remains an open question. Arkhipov et al. suggested this dipole makes exciton dissociation more efficient by preventing geminate pair recombination at the donor-acceptor interface.[8] It has also been suggested that the main cause of efficiency loss in excitonic solar cells is geminate pair recombination.[9] The binding energy of such geminate electron hole pairs across the interface has been reported to be approximately 0.3 eV.[10] Intuitively however, one would expect the electric field associated with the dipole to hinder the dissociation of an exciton due to electrostatic repulsion encountered by the hole and electron in the donor and acceptor materials respectively. The electric field points from positive to negative by definition and therefore its direction is from donor to acceptor. These ideas raise an important fundamental question relevant to the donor-acceptor interfaces in organic solar cells: what role, if any, does the interfacial electric field play in exciton dissociation and the overall quantum efficiency?

3.2 Experimental

The vibrational Stark effect becomes an important tool for the examination of the interfacial electric field. The carbonyl group of PCBM is an excellent reporter

for IR spectroscopy. Vibrational frequency shifts for functional groups in the presence of electric field have been attributed to the vibrational Stark effect for some time[11-13], most recently in work done by Pensack et al. for the PCBM/CN-MEH-PPV system.[14] For the BHJ device experiments, model devices were constructed using PCBM blended with choice donor polymers to simulate the active layer in BHJ devices. These blends were spun on top of a waveguide for study using multiple internal reflection Fourier transform IR (MIR-FTIR) spectroscopy. Fig. 3.2 shows the geometry of the model OPV device and the carbonyl signature of neat PCBM. The C=O stretching frequency for a neat film of PCBM is $\nu = 1736.5\ cm^{-1}$.

Several donor polymers were chosen for study for this work. P3HT is the standard material due to its high solubility, high hole mobility, and benchmark performance in organic devices. Other donor polymers such as poly(9,9′-dioctylfluorene-co-bis-*N*,*N*′-(4-butylphenyl)-bis-*N*,*N*′-phenyl-1,4-phenyldiamine) (PFB) and poly(2-methoxy-5-(2'-ethyl-hexyloxy)-1,4-phenylene vinylene) (MEH-PPV) were included as well due to recent studies.[9,15] Importantly, the donor polymer poly(9,9-di-*n*-octylfluorenyl-2,7-diyl) (F8) was included because it has been shown to have no vacuum level offset with respect to C_{60} since electron transfer from donor to acceptor for this system requires additional energy input.[7] Therefore, no interfacial dipole is expected to form for this system, and no Stark shift should be observed.

To fabricate model small molecule bilayer devices, molecules were thermally evaporated onto a germanium waveguide in high vacuum (10^{-7} Torr) at a rate of 1 Å s^{-1}. The edges of Ge waveguides were previously polished to 45° angles for use in

our MIR-ATR setup. 3,4,9,10-perylenetetracarboxylic dianhydride (PTCDA) was deposited along with the following small molecules: copper phthalocyanine (CuPc), 4,4'-N,N'-dicarbazolyl-biphenyl (CBP), N,N′-bis-(1-naphthyl)-N,N′-diphenyl1-1,1-biphenyl1-4,4′-diamine (α-NPD), tris-(8-hydroxyquinoline) aluminum (Alq_3) and bathocuproine (BCP).

PCBM was used as received from Aldrich and dissolved in 1,2-dichlorobenzene to a concentration of 20 mg mL^{-1}. P3HT (M_n = 19 kD, M_n = 43 kD, M_n = 76 kD) was used as received from Reike Metals and dissolved in 1,2-dichlorobenzene (20 mg mL^{-1}). Solutions were mixed and spin coated onto germanium substrates at 600 rpm. Neat PCBM was also spun at 600 rpm. Solutions of PFB, MEH-PPV, and F8 were 20 mg mL^{-1} in 1,2-dichlorobenzene. Mixing of solutions, spin coating, and FTIR were all performed in an N_2 glovebox with $[O_2]$ < 1 ppm. Thicknesses of blends were measured to be ~70 nm using ellipsometry (J. A. Wollam Co., Inc.) and profilometry (Tencor P-10).

PCBM and PCBM/P3HT blends were solvent annealed in 1,2-dichlorobenzene (Aldrich) vapor. The blends were removed from solvent anneal and IR spectra were recorded at certain time intervals. PCBM, PCBM/P3HT, PCBM/PFB, and PCBM/MEH-PPV were thermally annealed in a dry box at a temperature of 100˚C. The blends were removed at certain time intervals and spectra were recorded.

All spectroscopic measurements were performed on a Nicolet 6700 FTIR spectrometer. The IR beam was passed through a potassium bromide (KBr) window into a glove box and was focused by a concave mirror (f = 15 cm) into the

germanium waveguide. The exiting IR light was re-collimated and focused into a liquid nitrogen cooled Mercury Cadmium Telluride (MCT) infrared detector. AFM images were taken using tapping mode imaging with a Veeco Multimode V AFM under standard atmospheric conditions. The cantilever was driven off resonance to stabilize imaging with net repulsive force interactions. Both topography and phase images were collected to analyze contrasting material properties. The cantilever material was silicon nitride.

3.3 Results and discussion

3.3.1 *Vibrational Stark shift in model BHJ devices*

When PCBM is blended in a 1:1 ratio with donor polymer, a blue shift of 2.5 cm^{-1} is observed for PCBM blended with P3HT, PFB, and MEH-PPV. The notable exception is the F8/PCBM blend, which shows no shift with respect to neat PCBM. The data are shown in panel b of Fig. 3.3, and the amount of shift can be converted into a value for the interfacial electric field using the Stark tuning rate of 1 cm^{-1} (10^8 V m^{-1})$^{-1}$. This value was measured previously for acetone and methyl vinyl ketone.[16] The observed frequency shift gives an interfacial electric field of 0.25 V nm^{-1} for the PCBM/polymer systems (excluding F8). Recently, the critical electric field required to prevent 50% of geminate pair recombination was determined to be between 10^{-3} V nm^{-1} and 10^{-1} V nm^{-1} for varying blends.[9] Therefore as spun the blends tested here have electric fields above the critical field value. However, as spun blends have poor efficiency compared to annealed blends, suggesting higher interfacial electric fields have a negative impact on efficiency. No frequency shift is

observed for the F8/PCBM system, which means no interfacial electric field due to dipole formation is present at this interface. This result was earlier obtained by Osikowicz et al. for the similar C60/F8 interface.[7] The authors suggest integral charge transfer as the mechanism for dipole formation, as partial charge transfer would be unlikely to result in such a large interfacial field.[7] Using the simple model of a spherical capacitor with radius 1 nm and taking our measured interfacial electric field of 0.25 V nm^{-1}, the areal charge density was calculated to be 7.2E-4 C m^{-2}. Using r = 5 nm for a typical domain size,[17] the number of charges per domain is estimated to be ca. 1.4, supporting integral rather than partial charge transfer. The fact that in these data the entire carbonyl peak shifts and no broadening effect is present has been attributed to preferential alignment of molecules at the interface.[14]

3.3.2 *Annealing decreases interfacial electric field*

As spun blends are inefficient, and the effect of annealing the blends on device performance has been carefully studied, elucidating the most effective thermal annealing temperatures and times for certain donor polymers blended with PCBM.[17-19] In this work, samples of neat PCBM and PCBM/polymer blends were annealed in 1,2-dichlorobenzene vapor. Neat PCBM was solvent annealed for 1020 min, which led to the formation of a sharp, red-shifted peak at ν = 1730 cm^{-1} and a decrease in intensity of the neutral (ν = 1736.5 cm^{-1}) frequency. The ν = 1730 cm^{-1} peak is attributed to the formation of crystalline regions in the PCBM film upon annealing. The spectra of as-spun and annealed neat PCBM films are shown in Fig. 3.4. The fact that such a large effect on the carbonyl stretching frequency is

observed is at first surprising, because one would expect the negative charge density to be located almost entirely on the C_{60} and conjugation between C=O and C_{60} through the carbon tail would be unlikely. Rather, the red shift of the carbonyl stretch is due to charge transfer from electron rich portions of PCBM (the C_{60}) to the C=O on the PCBM tail through space.

PCBM crystallites have been previously observed upon solvent annealing,[20,21] and increased electron mobility and lifetime in the crystallites were demonstrated.[20] This implies that the result of annealing PCBM domains is more densely packed and ordered PCBM molecules. This situation allows for partial inter- or intra-molecular electron transfer through space. The sharpness of the red shifted portion of the carbonyl peak is in accord with this argument, because fewer conformations for the molecule would be favored in crystallites after annealing. The portion of the carbonyl peak which is not shifted is the result of amorphous PCBM in the blend.

In terms of morphology, the main effect of annealing PCBM/polymer blends comes from structural reorganization and ordering of the polymer phase with respect to the small molecule phase.[22,23] Here we suggest that polymer phase morphology, and more importantly, hole mobility on the polymer phase plays a crucial role in the strength of the interfacial electric field. First, we performed time-dependent annealing experiments on 1:1 blends of P3HT/PCBM systems with different P3HT molecular weights (M_n = 19 kD, M_n = 43 kD, M_n = 76 kD), referred to hereafter as low, mid, and high molecular weight. We observe a correlation between the amount of interfacial field loss and molecular weight of P3HT. This is visualized through

the change in vibrational Stark shift in Fig. 3.5, which shows IR spectra of P3HT/PCBM blends of low, mid, and high molecular weight P3HT as a function of annealing time. The crystalline phase of PCBM becomes present in the spectra at about 150 min annealing time, and its ratio relative to amorphous phase PCBM increases with annealing time. The data were fit using two Gaussian peaks to determine the position of the amorphous PCBM peak, and it was found that with increased annealing, the position of the amorphous peak changes. This effect is due to loss of the interfacial electric field with annealing. The extent to which the field is removed is a direct result of the extent of delocalization of the separated hole and electron. The interfacial electric field is removed more slowly for the high molecular weight P3HT/PCBM blends than for the lower molecular weight blends because it takes a longer time in solvent anneal to form ordered polymer domains with increasing molecular weight. Upon the formation of ordered domains, the extent of delocalization of the hole in the polymer phase increases. It has been suggested that higher annealing temperatures and longer annealing times are necessary to improve device performance with higher molecular weight P3HT.[24,25] Indeed, additional annealing (>2 days) of high molecular weight blends produced a shift back to neutral position of the amorphous PCBM C=O peak. As Fig. 3.5 shows, the ratio of crystalline to amorphous PCBM remains relatively constant regardless of P3HT molecular weight. Therefore, the crystallinity of the small molecule phases are similar. It should be noted that thermal annealing P3HT/PCBM blends produced the same results as solvent annealing. Because the strength of the electric field should not change with different molecular weight P3HT (due to similar charge carrier

mobilities measured for the different molecular weights),[24] and only an annealing time dependence was shown above, it becomes clear that the driving force for reduction of the interfacial electric field is a function of hole mobility in the polymer phase.

In addition to P3HT, donor polymers PFB and MEH-PPV were mixed with PCBM in a 1:1 ratio. As spun, Stark shifts of 2.5 cm^{-1} with respect to neat PCBM are observed as shown in Fig. 3.6. Differences arising from thermally annealing the blends can be attributed to different hole mobilities in the polymer phases. Similar results to the P3HT/PCBM systems are observed here as the crystalline phase of PCBM increases with annealing time for both PFB and MEH-PPV blends. However, for the PFB/PCBM system, after a thermal anneal time of 1035 minutes, the C=O of the amorphous PCBM has shifted back to the neat position. This is not the case for the MEH-PPV/PCBM blend, as after 1035 minutes of thermal anneal the Stark shift has only changed 1 cm^{-1}. Comparing the hole mobilities for the two polymers, a dependence on hole mobility was discovered. Hole mobility for PFB was previously determined experimentally by time of flight measurement to be 10^{-3} – 10^{-4} cm^2 V^{-1} s^{-1}.[26] This mobility is of similar magnitude to the hole mobility in low molecular weight P3HT/PCBM blends. The high hole mobility leads to movement of the charge throughout the bulk of the donor phase (away from the interface) and a subsequent decrease in the interfacial electric field. Hole mobility for MEH-PPV is lower than that for all molecular weight P3HT samples and PFB. The value was measured to be 10^{-7} cm^2 V^{-1} s^{-1},[27] and the electric field remains after annealing. These results strongly support the notion that the ability of the hole in the polymer

phase to move away from the interface is the biggest factor in determining the interfacial electric field in annealed devices.

This concept is illustrated schematically in Fig. 3.7. Panel a shows the HOMO, LUMO, and vacuum levels for a donor and acceptor material. When the two materials are mixed (panel b), negative charge transfer (integral) from donor to acceptor will occur until the charge transfer states of PCBM and polymer have equal energies.[7] Dipole formation therefore occurs. This dipole is the direct result of the transferred charge's inability to move away from the interface. The extent of crystallinity and mobility of the charge carrier for both the polymer and small molecule phases will determine the strength of the dipole and resulting electric field. Morphology of P3HT/PCBM films will be further discussed below. Annealing allows for further delocalization of the charges within crystalline domains and therefore a reduction in the interfacial field, which is schematically shown in Fig. 3.7 panel c. This reduction is directly related to the hole mobility in crystalline domains of the polymer phase. It is also a result of how well charge can move between neighboring domains. When the mobility of the hole is low (MEH-PPV), the geminate pair is more tightly bound to the interface as shown in panel d. In these cases, because the charges remain close to the interface, the interfacial electric field is present even after annealing. The geminate pair in this case will likely remain separated because of the high energetic barrier created by the electric field at the interface. While the field is in the direction prohibiting charge separation from an energetic point of view, it also prevents recombination once the charges are separated.

This electric field also hinders the dissociation of excitons into separate charge carriers due to its orientation. Positively charged carriers are bound in the donor material (and negatively charged carriers in the acceptor) near the interface, which will repel like charges and make exciton dissociation unfavorable. Delocalization of the charges in the high mobility cases upon annealing means the electric field decreases, but the Coulombic attraction between geminate pairs also decreases due to greater average distance between the carriers. This is the reason that in an actual device, charge transfer efficiency improves with annealing.

The morphology of the donor polymer also affects device performance through change in exciton binding energy. Calculations of exciton binding energies for 1D (e.g. as spun) and 3D (e.g. annealed) singlet excitons in the polymer phase show great reduction (in most cases) of the exciton binding in the 3D case versus the 1D case.[28] For polythiophene, the calculations by Shi et al. show that exciton binding energy decreases from 1.85 eV in the 1D case to ~0.4 eV in the 3D case.[27] Poly(acetylene) shows a similar effect. However, the calculations show very small change in exciton binding energy from 1D to 3D for PPV. In the presence of interfacial electric field, a tightly bound exciton will not be able to separate and likely recombine. In the same situation, an exciton with high 3D delocalization and low binding energy will likely separate, further decreasing the field. These calculations show just how important morphology is in determining device efficiency.

3.3.3 *Relation of film morphology to the interfacial electric field*

We examined the morphology of our P3HT/PCBM blends before and after annealing using AFM. Phase images of as spun low and high molecular weight blends show wormy features throughout both images (Fig. 3.8). For the high molecular weight blends, annealing causes significant morphology change. The height image (Fig. 3.8c) shows that the roughness increases by an order of magnitude, and the phase image shows clump like features rather than wormy features. This affect is due to ordering of the P3HT and crystallization of the PCBM clusters. The high molecular weight P3HT forms large crystalline domains and squeezes PCBM domains toward the surface.[22] The result is the clumps on worms motif imaged in Fig. 3.8b and illustrated in Fig. 3.8g. The morphology of annealed low molecular weight P3HT/PCBM blends is quite different as shown in Fig. 3.8e. The high image shows the same change in surface roughness observed for the high molecular weight blend, but the phase image lacks the features of the clumps on worms motif. It was recently concluded that PCBM and P3HT are well mixed upon annealing.[29] For the low molecular weight case, no clumping is observed due to smaller crystalline P3HT islands as illustrated in Fig. 3.8h. The ease of crystallization of the P3HT phase in the P3HT/PCBM blends is illustrated by the morphology measurements which directly correspond to the FTIR data shown in the previous section.

3.3.4 *Model bilayer OPVs made from small molecules*

Not only has the vibrational Stark effect been used to study electric fields in

BHJ OPV devices, but it could also be useful to study bilayer OPVs made from small molecules. Vázquez et al. have predicted the magnitude of the interfacial dipole formed between two organic small molecules with accuracy based on the charge neutrality level theory.[30-33] A similar suggestion (integer charge transfer) has also been proposed to explain the formation of the interfacial dipole.[7,34-36] The ideas are very different however, in the assumed interaction strengths at the interfaces. Integer charge transfer assumes Van der Walls type bonding and electronic coupling via tunneling.[7] Therefore, a much stronger interaction between the two organic semiconductors is assumed. Photoelectron studies by Osikowicz et al. have shown similar results for the interfacial dipole between C_{60} and P3HT, with the negative pole residing on the C_{60} phase.[7] The work in this section further explores the interfacial dipole using small molecule organic photovoltaic materials. This section presents preliminary data and serves as a starting point for using the vibrational Stark effect at organic small molecule interfaces.

The small molecule PTCDA was chosen for this research due to its good carbonyl reporter groups. The molecule is pictured in Fig. 3.9. As with PCBM, the carbonyl stretch frequencies of PTCDA will shift due to the vibrational Stark effect upon charge transfer at the organic – organic interface. The situation with PTCDA is slightly more complicated however, as there are four distinct vibrational frequencies corresponding to carbonyl stretches. The reason is symmetric and asymmetric stretches split into doublets.[37] PTCDA includes a symmetric and asymmetric C=O stretch. Additionally, the solid state effect known as Davydov splitting causes the doublet to split again. Davydov splitting is the result of adjacent molecules in the

unit cell having different orientations, resulting in each molecular vibration splitting into a doublet. This has been observed in pentacene molecular crystals.[38] The carbonyl stretches of PTCDA have been described by Tautz et al.[39] The four carbonyl stretches are shown in Fig. 3.10.

Bilayer devices were fabricated on top of germanium waveguides using PTCDA and a variety of other small molecules as illustrated in Fig. 3.11. The small molecule layers were deposited using thermal vapor deposition in high vacuum. The layer thicknesses were 5 nm. PTCDA bilayer devices were made using CuPc, CBP, α-NPD, Alq_3 and BCP. Multiple bilayers were formed in order to increase the signal-to-noise ratio. Upon bilayer formation, a shift in the position of the symmetric PTCDA carbonyl stretch is observed. Following the previous interpretation, the blue shift is due to an interfacial electric field. With respect to the carbonyl stretch of the neat PTCDA film, shifts of the bilayer devices are given in Table 3.1. Figure 3.12 shows the spectra corresponding to the values in Table 3.1. These data show that there exists a vibrational frequency shift after bilayer formation. However, it is unclear whether the shift is due to the Stark shift caused by an electric field between the PTCDA and small molecule interface, or a structural change upon bilayer deposition. Predicted and/or measured dipoles could validate the observed shifts, as would calculations for the carbonyl peak positions for charge PTCDA. The data shown in Fig. 3.12 and Table 3.1 do not follow predicted dipole trends,[32] so it is possible that a structural change is responsible for the vibrational frequency shifts. More controlled growth conditions will be required to further study small molecule interfaces.

3.4 Conclusions

In this work we measured the intrinsic electric field at donor acceptor interfaces based on the Stark effect on the C=O stretch vibrational peak of the PCBM molecule. It was found that upon mixing PCBM with a donor polymer, a field of 0.25 V nm^{-1} is present at the interfaces of PCBM with P3HT, PFB, and MEH-PPV. The field is due to electron transfer from donor to acceptor. No interfacial field exists for F8/PCBM blends, because charge transfer is an uphill process for this system. Thermal and solvent annealing of PCBM/polymer blends leads to ordering of both PCBM and polymer domains, as evidenced by FTIR and AFM. Depending on the mobility of the hole in the polymer phase, the interfacial electric field changes upon annealing.

The interfacial field is important as it serves two purposes. First, it prevents geminate pair recombination at the donor acceptor interface. This is the case because the interfacial dipole is larger than the Coulombic attraction between a geminate electron – hole pair. With annealing, the strength of the interfacial field decreases, making geminate pair recombination more likely. Second, the interfacial electric field is aligned so as to oppose exciton dissociation. Annealing PCBM/polymer blends removes the interfacial electric field to promote exciton dissociation. More charge carrier dissociation will occur with decreased interfacial electric field, but geminate pair recombination also becomes more likely. This work shows the importance of annealing PCBM/polymer blends not only from a morphological standpoint, but also from an energetic standpoint. For the formation of excitonic solar cell devices with the highest efficiencies, the optimal interfacial

energetics can be obtained through the extent of annealing. Finally, the mobility of the hole in the polymer phase should be taken into account as it affects magnitude of the interfacial electric field.

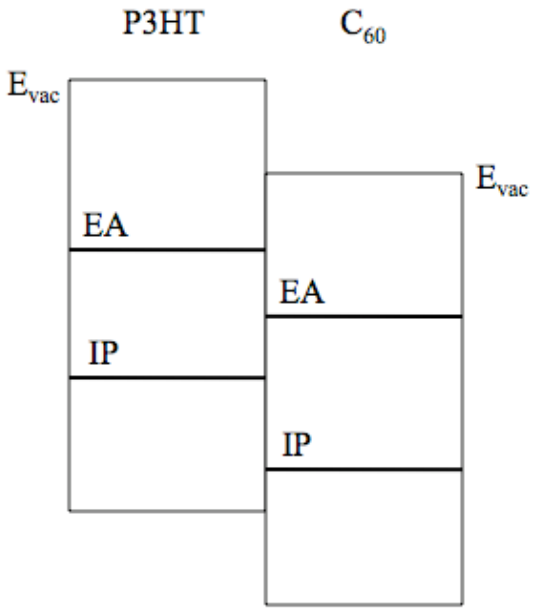

Figure 3.1 Vacuum level shift for a C_{60} – P3HT blend. The vacuum level refers to the energy level at which an electron is free from the solid. It also serves to define the molecule's electron affinity (EA) and ionization potential (IP).

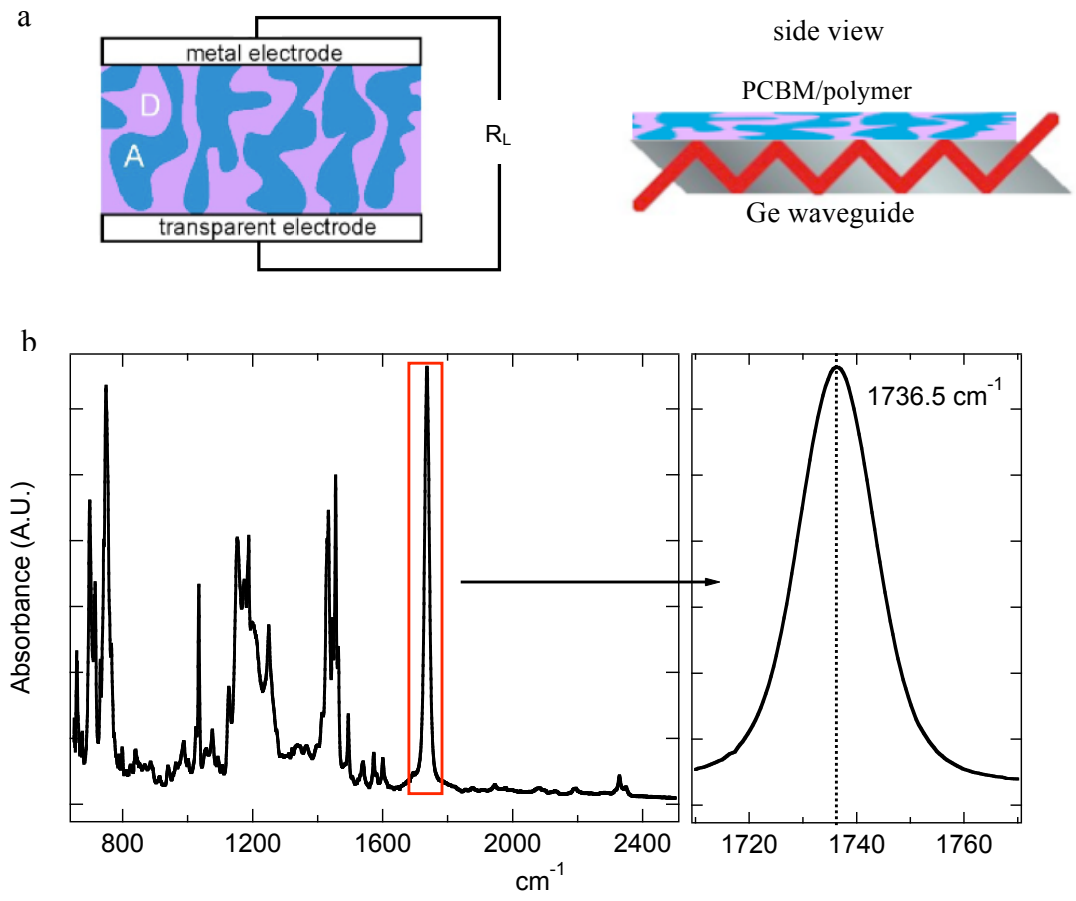

Figure 3.2 Geometry of model OPV device and carbonyl stretch. PCBM/polymer blend bulk heterojunction solar cells are modeled on top of an infrared waveguide as shown in panel a. Only the donor and acceptor blend is included in the model device. Panel b shows PCBM vibrational modes in the near IR region, with a zoom in of the carbonyl stretch at 1736.5 cm^{-1}.

a

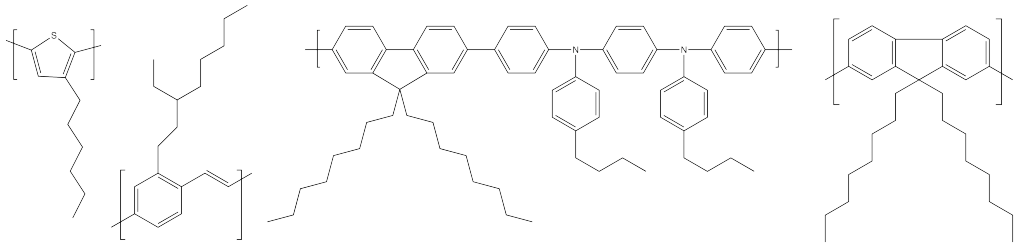

P3HT MEH-PPV PFB F8

b

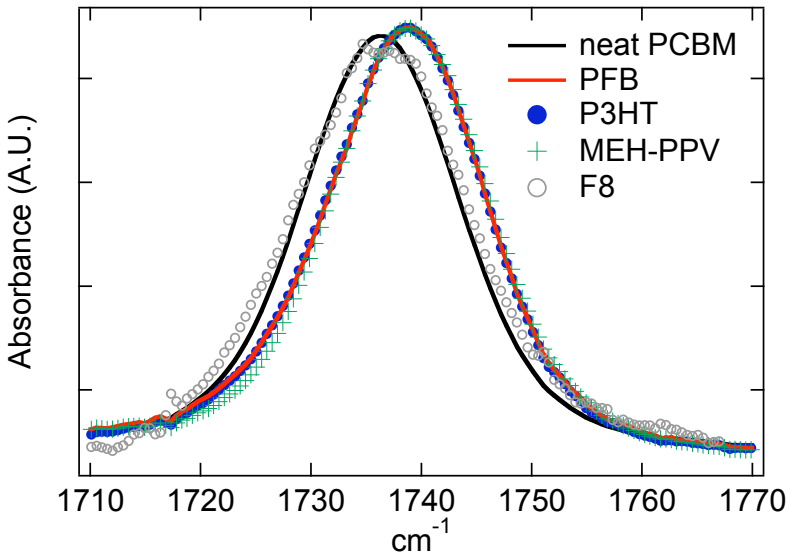

Figure 3.3 Structures of donor polymers and vibrational Stark shifts of BHJ blends. The various donor polymers examined with PCBM in this study are shown in panel a. As spun, PCBM blended with P3HT, PFB, and MEH-PPV exhibit a blue shift of the PCBM carbonyl of 2.5 cm^{-1} attributed the vibrational Stark effect due to the interfacial electric field. This is shown in panel b. The PCBM/F8 system shows no shift with respect to neat PCBM.

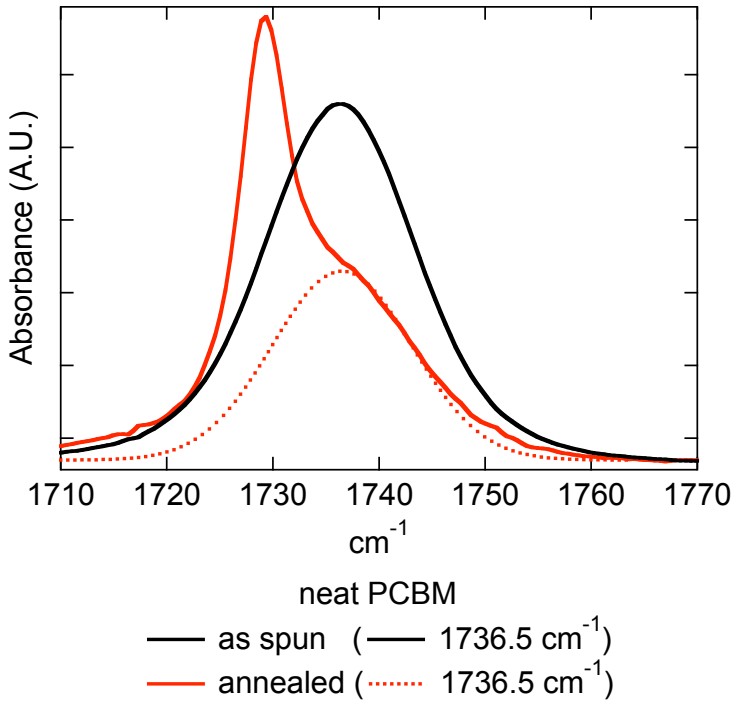

Figure 3.4 Annealing neat films of PCBM coincides with the growth of a peak at 1730 cm^{-1}. Ordering of PCBM with annealing causes both a red shift and narrowing of the carbonyl stretch. These effects are attributed to charge transfer through space from the electronegative C_{60} molecules to nearest carbonyl groups.

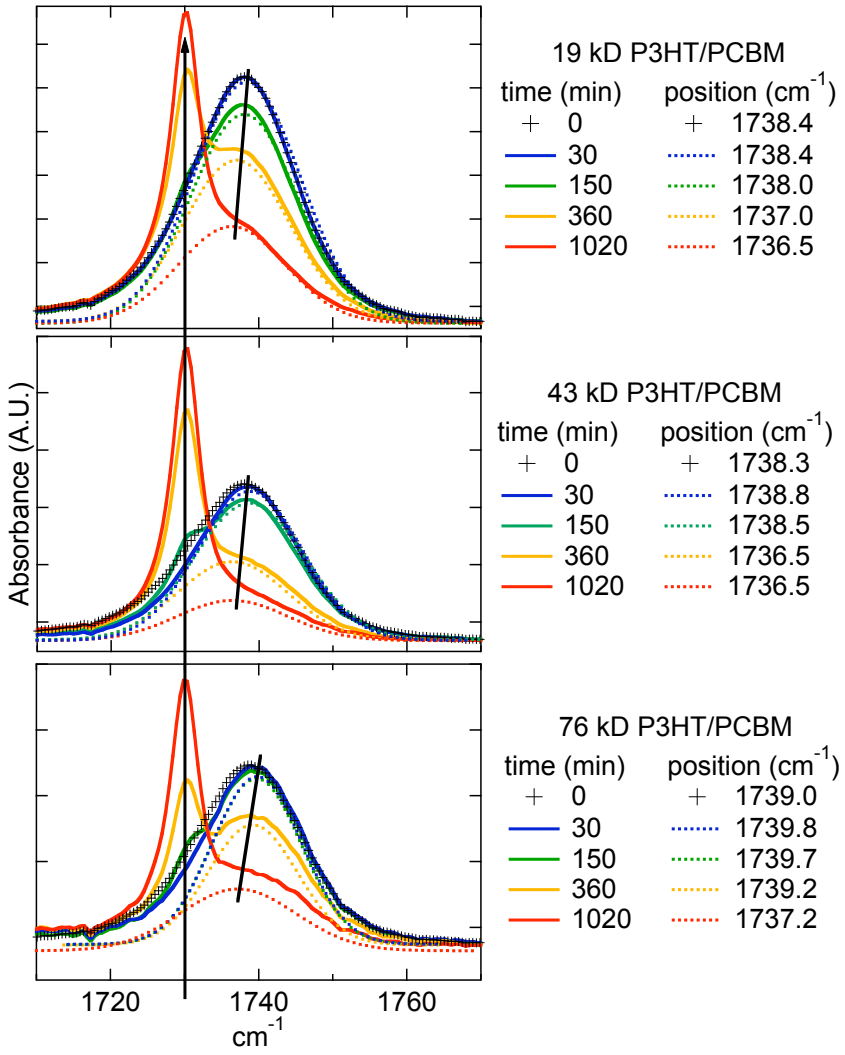

Figure 3.5 The vibrational Stark shift of the C=O PCBM stretch disappears with annealing time for P3HT/PCBM blends. For low molecular and mid weight P3HT/PCBM blends, the carbonyl stretch returns to its neutral position. For high molecular weight P3HT/PCBM blends, the vibrational Stark shift decreases with time, but at a slower rate.

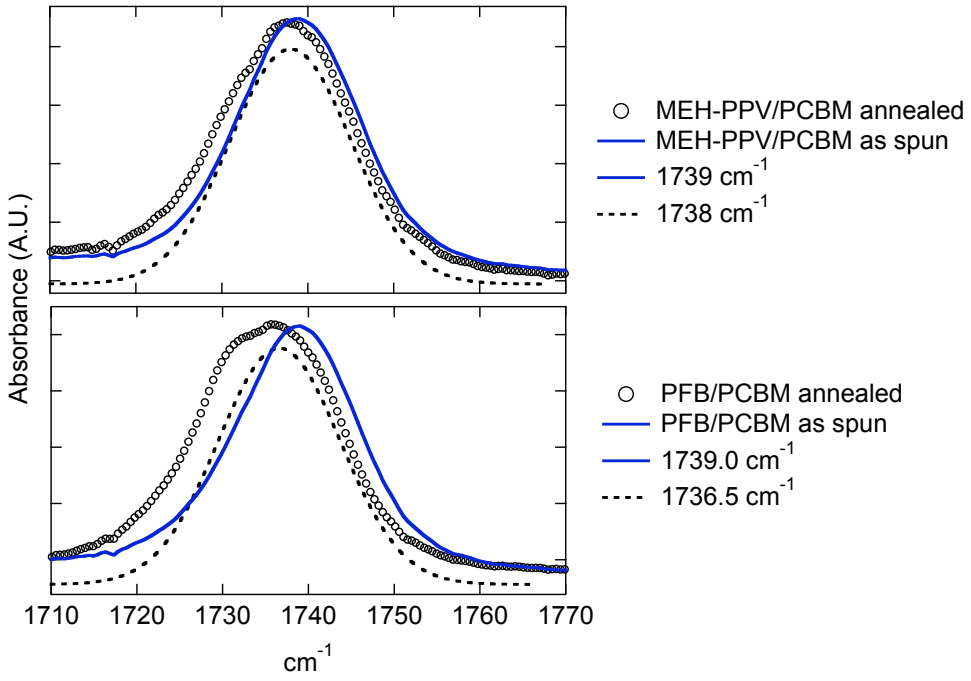

Figure 3.6 Annealing low molecular weight P3HT mixed with polymers MEH-PPV and PFB has different effects. The interfacial field diminishes with annealing time for PFB blends, but remains with MEH-PPV blends.

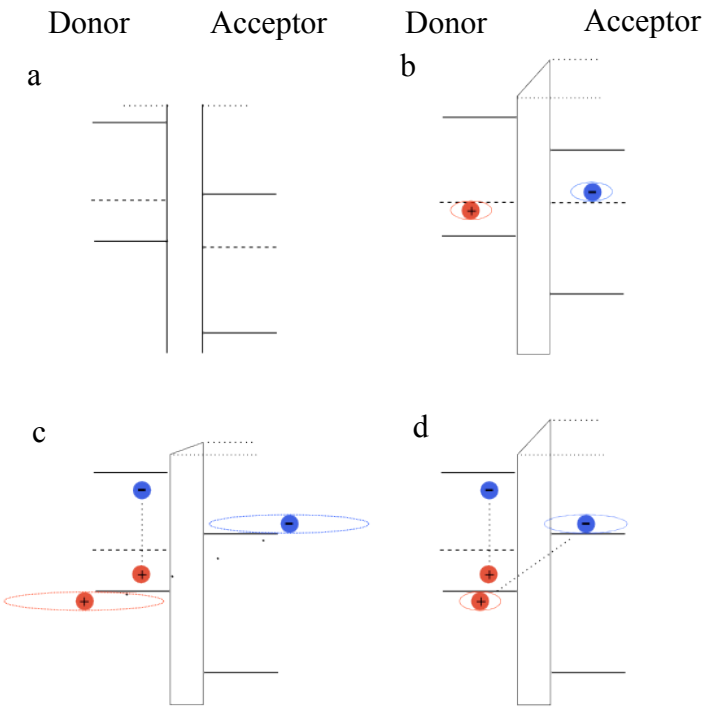

Figure 3.7 Initially, negative charge is transferred from donor to acceptor due to thermodynamic driving force. In as-spun blends, the charge is localized and the dipole creates an interfacial electric field. As the blends are annealed, the transferred charges delocalize; the extent of delocalization depends on the charge carrier mobility in the donor and acceptor phases. Panel c shows a hole and electron in an annealed blend. Since the charges are highly delocalized, the interfacial field is reduced. In panel d, the electron is delocalized but the hole remains localized in the polymer, so the interfacial field remains as the geminate pair is Coulombically bound.

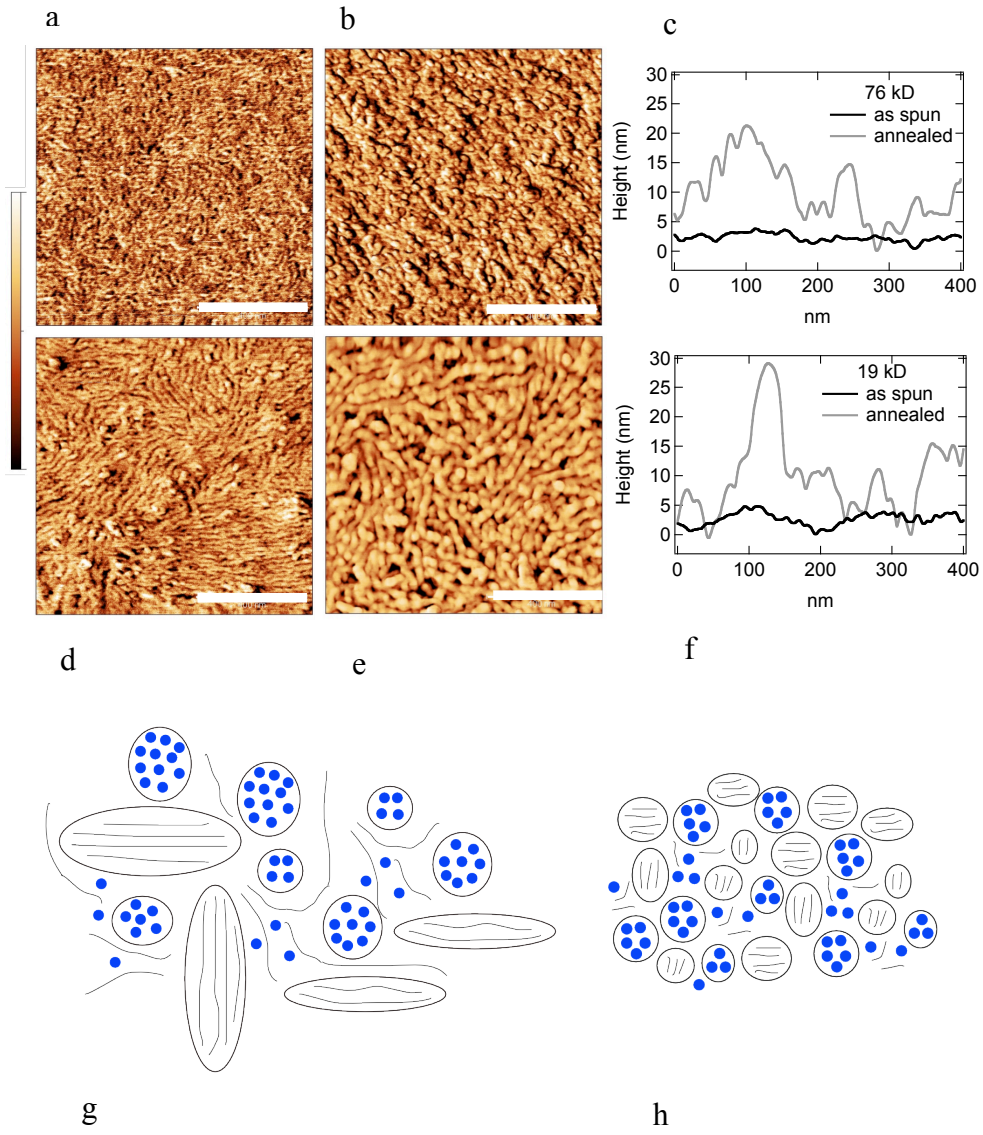

Figure 3.8 Phase images and line-scans for high molecular weight P3HT (a-c) and low molecular weight P3HT (d-f). Panels a and d are as for as spun films and b and e are annealed films. The height change upon annealing is similar for both molecular weights, but the morphologies are different. Cartoons (panels g-h) illustrate the morphologies observed for high and low molecular weight P3HT blends.

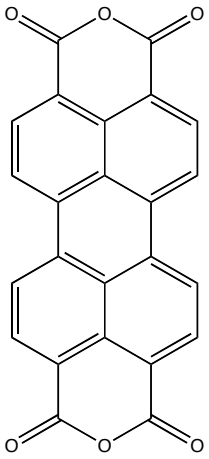

Figure 3.9 Small molecule perylene-3,4,9,10-tetracarboxylic-3,4,9,10-dianhydride (PTCDA) was chosen for this research due to its carbonyl reporter groups.

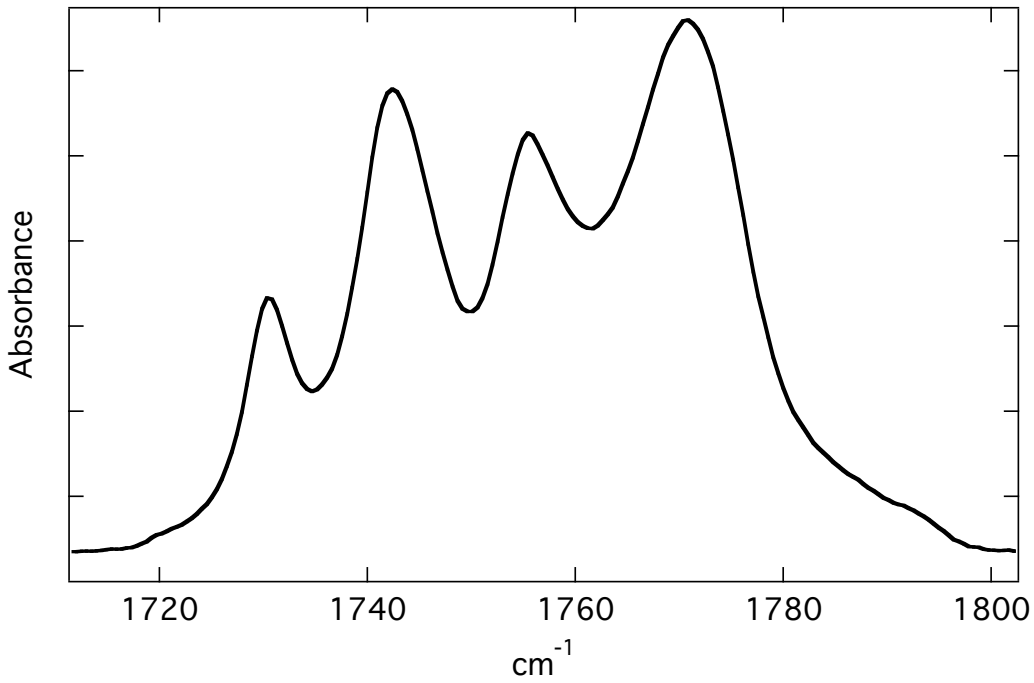

Figure 3.10 The carbonyl stretches of PTCDA. The C=O is split into a doublet due to symmetric and asymmetric stretching. Those stretches are also split into doublets because of Davydov splitting. The symmetric stretches are located at 1770 cm^{-1} and 1755 cm^{-1}, while the asymmetric stretches are at 1742 cm^{-1} and 1730 cm^{-1}. The peaks at 1755 cm^{-1} and 1730 cm^{-1} correspond to the inequivalent molecules in the unit cell.

Figure 3.11 Bilayer devices were fabricated on top of germanium waveguides. The devices included PTCDA and various small molecule semiconductors.

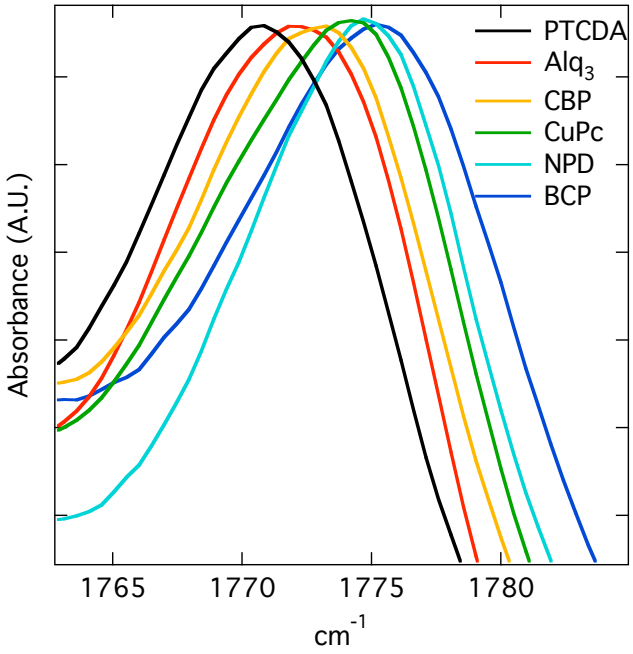

Figure 3.12 Symmetric carbonyl stretches for PTCDA deposited in bilayer geometry with small molecules.

Table 3.1 Vibrational frequency shifts for the carbonyl stretch of PTCDA bilayer devices with respect to the neutral (neat film ν=1770 cm^{-1}) position.

	CuPc	α-NPD	CBP	BCP	Alq_3
$\Delta\nu$ (cm^{-1})	4	5	3	5	2

3.5 References

[1] M. C. Scharber, D. Mühlbacher, M. Koppe, P. Denk, C. Waldauf, A. J. Heeger, C. J. Brabec *Adv. Mater.* **2006**, 18, 789.

[2] J. Xue, S. Uchida, B. P. Rand, S. R. Forrest *Appl. Phys. Lett.* **2004**, 85, 5757.

[3] V. I. Arkipov, H. Bässler *Phys. Status Solidi A* **2004**, 201, 1152.

[4] J. Y. Kim, S. H. Kim, H.-H. Lee, K. Lee, W. Ma, X. Gong, A. J. Heeger *Adv. Mat.* **2006**, 18, 572.

[5] G. Li, V. Shrotriya, J, Huang, Y. Yao, T. Moriarty, K. Emery, Y. Yang *Nat. Mater.* **2005**, 4, 864.

[6] Y. Kim, S. Cook, S. M. Tuladhar, S. A. Choulis, J. Nelson, J. R. Durrant, D. D. C. Bradley, M. Giles, I. McCulloch, C.-S. Ha, M. Ree *Nat. Mater.* **2006**, 5, 197.

[7] W. Osikowicz, M. P. de Jong, W. R. Salaneck *Adv*. *Mater*. **2007**, 19, 4213.

[8] V. I. Arkhipov, P. Heremans, H. Bäsler *Appl*. *Phys*. *Lett*. **2003**, 82, 4605.

[9] R. A. Marsh, C. R. McNeill, A. Abrusci, A. R. Campbell, R. H. Friend *Nano Lett.* **2008**, 8, 1393.

[10] H. Ohkita, S. Cook, Y. Astuti, W. Duffy, S. Tierney, W. Zhang, M. Heeney, I. McCulloch, J. Nelson, D. D. C. Bradley, J. R. Durrant *J. Am. Chem. Soc.* **2008**, 130, 3030.

[11] D. K. Lambert *Solid State Commun.* **1984**, 51, 297.

[12] A. Chattopadhyay, S. G. Boxer *J. Am. Chem. Soc.* **1995**, 117, 1449.

[13] L. N. Silverman, M. E. Pitzer, P. O. Ankomah, S. G. Boxer, E. E. Fenlon *J. Phys. Chem. B Lett.* **2007**, 111, 11611.

[14] R. D. Pensack, K. M. Banyas, L. W. Barbour, M. Hegadorn, J. B. Asbury *Phys. Chem. Chem. Phys.* **2009**, 11, 2575.

[15] L. W. Barbour, R. D. Pensack, M. Hegadorn, S. Arzhantsev, J. B. Asbury, *J. Phys. Chem. C* **2008**, 112, 3926.

[16] E. S. Park, S. G. Boxer *J. Phys. Chem. B* **2002**, 106, 5800.

[17] W. Ma, C. Yang, X. Gong, K. Lee, A. J. Heeger *Adv. Funct. Mater.* **2005**, 15, 1617.

[18] P. Schilinsky, U. Asawapirom, U. Scherf, M. Biele, C. J. Brabec *Chem. Mater.* **2005**, 17, 2175.

[19] X. Yang, J. Loos, S. C. Veenstra, W. J. H. Verhees, M. M. Wienk, J. M. Kroon, M. A. J. Michels, R. A. J. Janssen *Nano Lett.* **2005**, 5, 579.

[20] T. A. Bull, L. S. C. Pingree, S. A. Jenekhe, D. S. Ginger, C. K. Luscombe *ACS Nano*, **2009**, 3, 627.

[21] S. Nilsson, A. Bernasik, A. Budkowski, E. Moons *Macromolecules*, **2007**, 40, 8291.

[22] M. Campoy-Quiles, T. Ferenczi, T. Agostinelli, P. G. Etchegoin, Y. Kim, T. D. Anthopoulos, P. N. Stavrinou, D. D. C. Bradley, J. Nelson *Nat. Mater.* **2008**, 7, 158.

[23] G. Dennler, M. C. Scharber, C. J. Brabec *Adv. Mater.* **2009**, 21, 1.

[24] A. M. Ballantyne, L. Chen, J. Dane, T. Hammant, F. M. Braun, M. Heeney, W. Duffy, I. McCulloch, D. D. C. Bradley, J. Nelson *Adv. Funct. Mater.* **2008**, 18, 2373.

[25] R. C. Hiorns, R. de Bettignies, J. Leroy, S. Bailly, M. Firon, C. Sentein, A. Khoukh, H. Preud'homme, C. Dagron-Lartigau *Adv. Funct. Mater.* **2006**, 16, 2263.

[26] R. U. A. Kahn, D. Poplavskyy, T. Kreouzis, D. D. C. Bradley *Phys. Rev. B* **2007**, 75, 035215.

[27] Q. Shi, Y. Hou, J. Lu, H. Jin, Y. Li, Y. Li, X. Sun, J. Liu *Chem. Phys. Lett.* **2006**, 425, 353.

[28] K. Hummer, P. Puschnig, S. Sagmeister, C. Ambrosch-Draxl *Mod. Phys. Lett. B* **2006**, 20, 261.

[29] W. Ma, J. Y. Kim, K. Lee, A. J. Heeger *Macromol. Rapid Commun.* **2007**, 28, 1776.

[30] H. Vázquez, R. Oszwaldowski, P. Pou, J. Ortega, R. Perez, F. Flores, A. Kahn *Europhys. Lett.* **2004**, 65, 802.

[31] H. Vázquez, F. Flores, R. Oszwaldowski, J. Ortega, R. Perez, A. Kahn *Appl. Surf. Sci.* **2004**, 234, 107.

[32] H. Vázquez, W. Gao, F. Flores, A. Kahn *Phys. Rev. B* **2005**, 71, 041306.

[33] A. Kahn, W. Zhao, W. Gao, H. Vázquez, F. Flores *Chem. Phys.* **2006**, 325, 129.

[34] C. Tengstedt, W. Osikowwicz, W. R. Salaneck, I. D. Parker, Che-H. Hsu, M. Fahlman *Appl. Phys. Lett.* **2006**, 88, 053502.

[35] S. Braun, W. Osikowicz, Y. Wang, W. R. Salaneck *Org. Electron.* **2007**, 8, 14.

[36] A. Crispin, X. Crispin, M. Fahlman, M. Berggren, W. R. Salaneck *Appl. Phys. Lett.* **2006**, 89, 213503.

[37] B. Smith *Infrared Spectral Interpretation: A Systematic Approach* **1998** (CRC Press).

[38] H.-L. Cheng, W.-Y. Chou, C.-W. Kuo, Y.-W. Wang, Y.-S. Mai, F.-C. Tang, S.-W. Chu *Adv. Funct. Mater.* **2008**, 18, 285.

[39] F. S. Tautz, S. Sloboshanin, J. A. Schaefer, R. Scholz, V. Shklover, M. Sokolowski, E. Umbach *Phys. Rev. B.* **2000**, 61, 16933.

Chapter 4. Polaron and ion diffusion in a poly(3-hexylthiophene) thin film transistor gated with polymer electrolyte dielectric

4.1 Introduction

Electrolytes are finding applications as dielectric materials in low-voltage organic thin film transistors (OTFT). The presence of mobile ions in these materials (polymer electrolytes or ion gels) gives rise to very high capacitance (>10 μF cm^{-2}) and thus low transistor turn-on voltage. In order to establish fundamental limits in switching speeds of electrolyte gated OFETs, we carry out in situ optical spectroscopy measurement of a poly(3-hexylthiophene) (P3HT) OTFT gated with a $LiClO_4$:poly(ethyleneoxide) (PEO) dielectric. Based on spectroscopic signatures of molecular vibrations and polaron transitions, we quantitatively determine charge carrier concentration and diffusion constants. We find two distinctively different regions: at $V_G \geq$ -1.5 V, drift/diffusion (parallel to the semiconductor/dielectric interface) of hole-polarons in P3HT controls charging of the device; at $V_G <$ -1.5 V, electrochemical doping of the entire P3HT film occurs and charging is controlled by drift/diffusion (perpendicular to the interface) of ClO_4^- counter ions into the polymer semiconductor.

Polymer electrolytes consisting of mobile ions dissolved in a polymer matrix[1] are being explored as high-capacitance dielectric materials for OTFTs.[2-6] The effective capacitance of these materials can be as high as 10^3 times those of conventional dielectrics. Such exceptionally high capacitance (>10 μF cm^{-2}) is believed to come from the diffusion of mobile ions to the dielectric/organic

semiconductor interface upon the application of a gate voltage, resulting in the formation of an electrical double layer with nanometer thickness. This high capacitance permits very low gate voltage in switching an OTFT from the off-state to the on-state, as demonstrated by a number of groups for OTFTs based on organic single crystals[2,3] and small molecule[4] or polymer[5,6] semiconductor thin-films. A fundamental question of interest here concerns the mechanism of charge injection: Is the gating process purely electrostatic or electrochemical?

We define electrostatic doping as a distinct interface with mobile ions of one polarity accumulating on the polymer electrolyte side and charge carriers of opposite sign accumulating on the organic semiconductor side. The electrostatic doping mechanism occurs for a very thin portion (e.g., approximately a single layer) of the organic semiconductor layer immediately next to the dielectric where the electrostatic field is highest. In contrast, an electrochemical doping process can be defined as the mass transfer of mobile ions into the bulk of the organic semiconductor. In this case, the entire organic semiconductor sample (the total thickness of the thin film) can be doped. The electrochemical mechanism is unambiguous at high gate voltages, as the total injected charge density is well beyond what can be accommodated by one or a few molecular layers. There are also distinct spectroscopic signatures associated with electrochemical doping.[7,8] In comparison, the electrostatic doping mechanism usually believed to be operative at low gate bias is less black-and-white in some cases. For example, the simple picture of an electrical double layer may apply for OTFTs based on organic single crystals, as the penetration of ions into the organic semiconductor is hindered by the close-

packed crystal structure. However, roughness and a distribution of structural defects at the surface of a molecular or polymer film may permit the diffusion or partial penetration of ions into the first layer of the organic semiconductor phase. This process resembles the electrochemical mechanism, but only for the interface region of the organic semiconductor (not the entire film). Thus, a clear distinction between electrostatic or electrochemical doping is neither necessary nor warranted in this case.

Despite the ambiguity in doping mechanisms of OTFTs gated with polymer electrolyte dielectrics, a question of more practical importance is very clear: *what is the rate-limiting step in charge injection/accumulation?* This charging rate determines the maximum switching speed of an OTFT. There are three drift/diffusion processes; each may limit the charging rate: the drift/diffusion of anions or cations in the polymer electrolyte towards the organic semiconductor interface, the drift/diffusion of ions into the organic semiconductor, and the drift/diffusion of charge carriers in the conducting channel of the organic semiconductor. The first process is the effective dielectric response of the polymer electrolyte. As we show in this report, the movement of ions in the polymer electrolyte is not rate-limiting. The second (ion penetration) or the third (carrier movement) process can be rate limiting, depending on the extent of electrochemical doping and dimension of the conducting channel. We use regio-regular poly(3-hexylthiophene) (P3HT) as the polymer semiconductor and a solid state solution of $LiClO_4$ in poly(ethyleneoxide) (PEO) as the gate dielectric, as this model system has been thoroughly investigated recently in transistor measurements.[5-7] Panzer and

Frisbie showed that the mobile ions in the PEO-$LiClO_4$ dielectric provided a very high capacitance which enabled a low turn on voltage of V_G = -1.5 V for the P3HT transistor.[5] Temperature dependent measurements showed little thermal activation for charge transport in the on-state (V_G < -1.5 V); this led to the suggestion that the high conductivity state for V_G < -1.5 V was metallic like. A similar conclusion was reached by Heeger and coworkers in a transistor measurement using the same PEO-$LiClO_4$ dielectric with P3HT and a different polythiophene;[6,8] these authors concluded that electrochemical doping was responsible for the high-conductivity state. We recently carried out in situ optical spectroscopy measurements of gate-doped P3HT using the PEO-$LiClO_4$ dielectric and found that, in the insulating state at low doping level, hole polarons were present in two distinct environments: crystalline and amorphous phases of P3HT. In the metallic region at high doping levels, the two polaron states merge into a single state. We took this as evidence for strong carrier screening which removed the energetic barrier for polaron transfer from crystalline to amorphous domains and was responsible for the insulator-to-metal transition.[9] The present study focuses on the rate limiting steps in charge build-up in the polymer electrolyte gated device.

4.2 Experimental

All devices used in this study were fabricated on silicon crystals that served as waveguides for multiple internal reflection Fourier transform infrared (MIR-FTIR) spectroscopy. Each Si crystal (10mm x 32 mm x 1mm) was cut from a lightly doped silicon wafer and polished to the shape of a parallelogram with 45˚ angles

forming the two ends of the parallelogram. Each device, shown schematically in Figure 1, was fabricated in inert environment (N_2 drybox or vacuum) on native oxide terminated Si as follows. A P3HT thin film (MW = 55 kD, Rieke Metals) was spin-coated from a 20 mg mL^{-1} solution in 1,2-dichlorobenzene (Sigma) onto the Si surface. The P3HT film thickness was 190 ± 10 nm, as determined by profilometry (Tencor P10). A 30 nm thick Au source/drain electrode array (each 1.6 cm in length) was then thermally evaporated in a vacuum chamber ($1x10^{-6}$ Torr) onto the P3HT film. We used three different arrays: the first having 12 Au electrodes (11 channels) with inter-electrode spacing (i.e. channel length) of L_c = 0.50 mm; the second consisting of 5 Au electrodes (4 channels) with L_c = 1.06 mm; the third of two electrodes (one channel) with L_c = 7.25 mm. Following the deposition of Au electrode array, we deposited (drop-casting in acetonitrile) a 100 μm thick polymer electrolyte gate dielectric, which consisted of $LiClO_4$ in PEO (MW = 10^5) in a ratio of 16 ether oxygen atoms per lithium ion. We completed each device by thermally evaporating a 30 nm thick Au gate electrode (1.6 cm^2) onto the polymer electrolyte dielectric. The active (gated) areas of P3HT were 0.88 cm^2, 0.68 cm^2, and 1.16 cm^2 for devices with L_c = 0.50, 1.06, and 7.25 mm, respectively.

We carried out all spectroscopic measurements on a Nicolet 6700 FTIR spectrometer. The IR light was passed through a KBr optical window into a glove box (O_2 concentration < 0.1 ppm) and was focused by a concave mirror (f = 15 cm) into the silicon waveguide of the OTFT device. The exiting IR light was re-collimated and focused into a liquid nitrogen cooled Mercury (Hg) Cadmium (Cd) Telluride (Te) (MCT) infrared detector. For in-situ spectroscopic measurements, the

source and drain electrodes were both grounded while a negative bias was applied to the gate. The gate current was recorded on a Keithley 6517A electrometer. We present each MIR-FTIR spectrum on an absorbance scale using a bare Si waveguide as background.

A typical absorbance spectrum at V_G = -1.5 V is shown in the lower part in Fig. 4.1. There are two main features in this spectral region: a sharp vibrational peak at 1510 cm^{-1} due to the ring stretching mode (ω_R) of neutral thiophene[10] and a broad peak centered around ~3800 cm^{-1} due the HOMO → polaron electronic transition (ω_1).[11,12] Note that the infrared active vibrational modes (IRAV)[13] are at lower frequency than that of ω_R and are obscured by the strongly absorbing phonon modes of SiO_2. We find that the intensity of the ω_R peak decreases with increasing doping (more negative gate voltage) due to the conversion of neutral thiophene molecules to the positively charged radical cation (hole polaron). As expected, the intensity of the polaron peak (ω_1) increases with doping. We will rely on these two peaks for the quantification of hole polarons in P3HT.

4.3 Results and Discussion

4.3.1 *Quantitative determination of hole concentration in gate-doped P3HT*

Previous transistor measurements on P3HT OTFTs gated with the PEO-$LiClO_4$ dielectric showed a low transistor turn on voltage of V_G = -1.5 V.[5] When the transistor is switched to the on-state (V_G < -1.5 V), there was orders-of-magnitude increase in charge carrier concentration and channel conductivity. In the present study, we focus on carrier injection mechanisms at or above this transition

voltage. Upon application of a gate voltage ($V_G < 0$), we record in-situ FTIR spectra and measure gate current (I_G) simultaneously as a function of time. The electrical and spectroscopic measurements can then be quantitatively compared. The upper panel in Fig. 4.2 shows time-dependent gate current for the wide channel device (L_C = 7.25 mm) after V_G is switched from 0 to -1.50 V at t = 0. The integration of I_G corresponds to the total charge, *Q(t)*, injected into the active area of the P3HT film, assuming that leakage current is negligible. The validity of this assumption is supported by the low level of I_G at the long time limit, by the negligible I_G at lower gate bias (data not shown), and by the excellent agreement between gate current and spectroscopic measurements. The latter is shown in the lower panel, which compares the injected charge density (red curve, *Q(t)*, obtained from integrated I_G) with the peak area (crosses) for the polaron transition (see ω_P in Fig. 4.1). Similar agreements are obtained for devices of smaller channel width. We thus reliably obtain a calibration factor to convert ω_1 absorption to hole polaron concentration.

Another spectroscopic signature associated with charge accumulation in the P3HT film is the loss of peak intensity in the neutral thiophene ring stretching mode, as illustrated by the inset in the lower panel of Fig. 4.2. Based on the percentage loss of peak intensity, the total injected charge density, a thiophene monomer concentration of 5.2×10^{21} cm^{-3} (from the thin film density of 1.33 g cm^{-3}),[14] and the percentage of active area under gate bias, we estimated that each injected hole corresponds to the intensity loss of 19 ± 10 thiophene rings, in agreement with the reported size of the hole polaron in P3HT from electron-nuclear double resonance measurements.[15]

4.3.2 *Polaron or counter ion drift/diffusion can be rate-limiting.*

The major factors controlling the rate of charge accumulation are the drift/diffusion of charge carriers in the conducting channel of the organic semiconductor and the drift-diffusion of ions into the organic semiconductor. The drift-diffusion of the ions inside the polymer electrolyte is ruled out as a rate limiting process later with simulation. To determine whether ion drift-diffusion into the semiconductor or carrier drift-diffusion is the rate limiting process, we compared devices of different channel widths. For a charging process controlled by carrier movement parallel to the interface, the charging rate should depend on channel width of the device. In contrast, a charging process controlled by ion penetration into the organic semiconductor layer is independent of channel width since all devices probed here possess the same organic semiconductor thickness. The upper panel in Fig. 4.3 shows the polaron uptake curves for three different channel lengths (L_C = 0.50, 1.06, 7.25 mm) at V_G = -1.5 V. Each data point is obtained from the ω_1 peak area in FTIR spectra. The polaron concentrations are presented in both area density and volume density based on the measured film thickness of 190 nm. The maximum hole density achievable at this gate bias is 2.5×10^{15} cm^{-2}, which is ~3x the density of thiophene rings in a monolayer (assuming a thickness of a = 16.63 Å for the crystalline domains).[16] Thus, charging of the device at this gate bias occurs well beyond the first layer of thiophene units in contact with the dielectric. We call doping at or below the transition gate voltage "light" electrochemical doping. Charging in this "light" electrochemical doping region is rate-limited by carrier diffusion from the source/drain electrodes as established by the channel length

dependence. For the short channel device (L_C = 0.5 mm), we see saturation of the injected carrier density for $t \leq 1x10^3$ s. At saturation, charge neutrality is achieved in the P3HT where each hole polaron is balanced by a ClO_4^- ion.[17] The saturation level is not reached within the timeframe of the measurements for the medium and long channel devices. Since, the source-drain voltage is zero (both electrodes grounded) in our measurement, hole polaron movement can be approximated by one-dimensional (1D) diffusion from the two electrodes. Solution to the 1D diffusion problem (from two boundaries) is known:[18]

$$Q(t) = C - \frac{2C}{\pi}\sum_{n=1}^{\infty}\left(\left(\frac{2}{(2n-1)^2\pi}\right)\exp\left(-(2n-1)^2\pi^2\frac{Dt}{l^2}\right)\right), \quad (1)$$

where C is saturation concentration at $t \to \infty$; D is the diffusion constant; l is the channel length. The three red curves in the upper panel of Fig. 4.3 are fits to equation (1) for the three different channel lengths. These fits give a diffusion constant for the hole polaron of D_h = 1.1 ± 0.4 x 10^{-6} cm^2 s^{-1}, independent of the channel length of the device. The latter supports the interpretation that hole diffusion in the channel is rate-limiting. Similar results are observed for -1.5 V < V_G < -1.0 V (data not shown).

When the gate voltage is increased to V_G = -2.0 V, there is a dramatic increase in the amount of charge injected; this is consistent with previous transistor measurements. The hole polaron density at V_G = -2.0 V is over 50 times that at V_G = -1.5 V. The maximum hole polaron density is ~$6x10^{21}$ cm^{-3} at the long time limit.

This maximum density is greater than the total thiophene ring density and is therefore probably an overestimation. The cause of this overestimation is likely due to the failure of the factor used to convert polaron absorbance into charge carrier density at high carrier densities. The factor itself depends on carrier density, which makes the conversion unreliable at higher gate voltages. Gate voltage dependence stems from the fact that the absorption cross section for the ω_P absorption most likely changes as the system passes through the metal-to-insulator transition which occurs between -1.5 and -2.0 V.[9] Regardless of the exact carrier density, virtually the entire P3HT film is doped electrochemically. There must be significant electronic interaction and charge carrier screening among hole polarons at such a high doping level. Note that, due to slowness in charging rate, the amount of charge injection is a strong function of time or switching frequency. The total charge injected at the long time limit is 2-3 orders of magnitude higher than that reported earlier for much shorter time scales.[5]

The uptake curves of the two short channel devices (L_C = 0.50 and 1.06 mm) are nearly identical within experimental uncertainty. This establishes that diffusion of counter ions (ClO_4^-) through the P3HT film is rate limiting. To the first approximation, we use a simple 1D diffusion model (from the dielectric interface into the 190 nm thick P3HT film) to describe the charging curves. The fits give a diffusion constant of D_{Ion} = 1.3±0.1 x10^{-14} cm^2 s^{-1}. For comparison, Kaneto et al. reported ClO_4^- diffusion constants of 10^{-12}-10^{-10} cm^2 s^{-1} in a polythiophene film in contact with liquid electrolyte.[19] The low diffusion constant for ClO_4^- through the

semiconducting polymer film is responsible for the slow kinetics of electrochemical doping.[19- 21]

When the channel length is increased to 7.25 mm, the charging rate is much lower than at shorter channel lengths. Thus, at this voltage, the rate-limiting step changes from diffusion of ions (perpendicular to the semiconductor/dielectric interface) at short channel length (L_C = 0.50 and 1.06 mm) to hole diffusion along the channel at long channel length (L_C = 7.25 mm). Fitting the charging curve at L_C = 7.25 mm to equation (1) gives a hole polaron diffusion constant of D_h = 6.8 ± 0.9 x 10^{-6} cm^2 s^{-1}. The hole diffusion constant at V_G = -2.0 V is 6x times that at V_G = -1.5 V, consistent with the well-known fact that carrier mobility in an OTFT increases with doping level, including electrochemically doped P3HT.[5,22] This is often explained by the presence of a distribution (in terms of energy) of charge carrier traps in the organic semiconductor. According to the multiple trap and release (MTR) model of charge transport in organic semiconductors, as gate voltage is increased and more charges are injected into the semiconductor, traps are filled (from deep to shallow) and activation energy for the release of a carrier out of a trap decreases.

To the first approximation, we can relate the hole diffusion constant to mobility based on the Einstein relationship:

$$\frac{D}{\mu} = \frac{kT}{q}, \tag{4.2}$$

where D is the diffusion constant; μ is the mobility; k is Boltzmann's constant; T (= 295 K) is temperature, and q is the charge of the carrier. The diffusion constant at V_G = -2.0 V corresponds to a mobility of μ = 2.7 x 10^{-4} cm^2 V^{-1} s^{-1}, which is similar to those reported in transistor measurement for P3HT gated with the PEO-$LiClO_4$ dielectric.[5,22] Note that, for more quantitative conversion, correction to the Einstein relationship must be included to account for the presence of a distribution of traps.[23]

A consistent picture emerging from the above measurements is as follows. Charging of the polymer semiconductor due to electrochemical doping is determined by the diffusion/drift of both charge carriers and counter ions, the former from source/drain electrodes and the latter from the polymer electrolyte dielectric. Each of these two processes can be rate limiting, depending on device geometry and the extent of doping. For low to moderate levels of electrochemical doping, counter ion penetration into the interface and near-interface region is faster than the diffusion of holes on the semiconductor. The presence of excess counter ions in the organic semiconductor provides driving force for the injection of charge carriers into the channel and diffusion or drift (if a source-drain bias is applied) of charge carriers is the rate-limiting step. For high levels of electrochemical doping, either drift/diffusion of counter ions or charge carriers can be rate-limiting, depending on the channel length to thickness ratio. For complete electrochemical doping at short channel length, drift/diffusion of ions through the organic semiconductor film is rate-limiting, while at long channel length, drift/diffusion of carriers becomes rate-limiting.

4.3.3 *Polarization of the polymer electrolyte is fast.*

The analysis shown above is based on the assumption that ion movement within the polymer electrolyte is faster than ion or hole drift/diffusion in the polymer semiconductor. To determine the timescale of polarization of the PEO-$LiClO_4$ dielectric material, we carry out modeling using a finite element method within the COMSOL Multiphysics package. The differential equations governing the motion of ions in the dielectric are solved numerically for a finite number of spatial points. The equations used take ion diffusion and their interaction with the applied electric field into consideration. The values used for the diffusivity of the lithium and perchlorate ions are from previous measurements.[1,24] In order to solve Poisson's equation self-consistently with the electric field, we impose a maximum concentration boundary condition. This condition forces the diffusivity and the field effect mobility to approach zero as the ion concentration reaches the specified maximum concentration. Concentration dependent conductivity is well documented and can be understood by noting that ion conduction requires both ions and ion vacancies. The value used as the maximum concentration is obtained by assuming that the concentration of ether oxygen atoms in PEO must be at least four times the lithium ion concentration. That is, the lithium ions must be coordinated by at least four ether oxygen atoms.[25] To give this condition physical relevance, we take the finite element mesh to represent the average spacing between ether oxygen atoms.

Fig. 4.4 represents the time dependent evolution of perchlorate ion concentration at the semiconductor/dielectric interface after the gate voltage is turned on at t = 0. The most obvious conclusion is that polarization of the dielectric occurs

at a time scale close to μs, much faster than the timescales of charge injection. Thus, the time dependent responses observed from gate current and spectroscopic measurements are not due to ion motion in the PEO dielectric material. This conclusion may initially seem surprising, given the relatively low conductivity of the PEO/$LiClO_4$. However, the apparent puzzle is resolved when we consider the small distances the perchlorate ions near the interface must traverse to establish their equilibrium concentration profile. This distance should be on the order of the Debye screening length ($\lambda_D \approx$ a few Å).

4.4 Conclusions

We carried out in situ optical spectroscopy measurement of a P3HT OTFT gated with a $LiCl_4$:poly(ethyleneoxide) (PEO) dielectric with different channel lengths. There are two electrochemical doping mechanisms. At $V_G \leq$ -1.5 V, drift/diffusion of hole-polarons in the P3HT channel controls charging of the device while at V_G = -2.0 V, charging is controlled by drift/diffusion (perpendicular to the interface) of ClO_4^- counter ions into the polymer semiconductor for short channel length devices. However, hole polaron motion can again be rate-limiting if the channel length is sufficiently long. The hole diffusion constants are D_h = 1.1±0.4 x10^{-6} and 6.8±0.9 x 10^{-6} cm^2 s^{-1} at V_G = -1.5 V and -2.0 V, respectively. The diffusion constant of the ClO_4^- counter ions in P3HT is much slower, D_{Ion} = 1.3±0.1 x10^{-14} cm^2 s^{-1}.

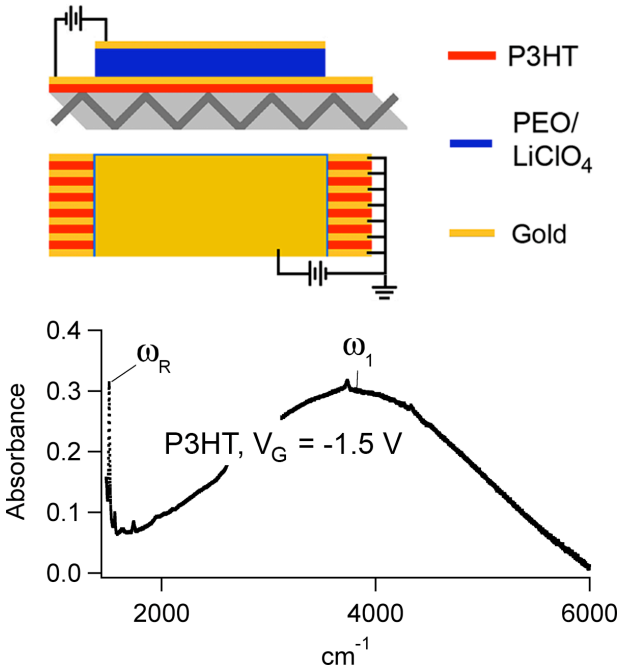

Figure 4.1 Upper: Schematic illustration of the P3HT OTFT gated with LiCl4-PEO polymer electrolyte dielectric on an IR waveguide. Lower: In situ FTIR spectrum obtained at V_G = -1.5 V. ω_R (= 1510 cm^{-1}) is the ring stretching vibrational mode neutral thiophene; ω_1 (~3800 cm^{-1}) is the HOMO → polaron transition.

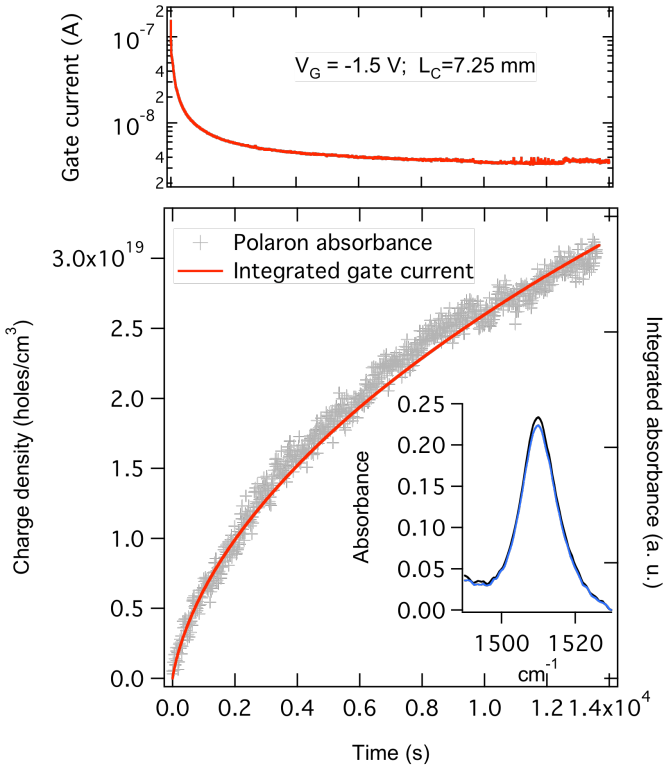

Figure 4.2 Upper: Gate current (I_G) of the wide channel device (L_C = 7.25 mm). Lower: total injected charge obtained from the integrated gate current (red) and peak area of the ω_P polaron transition (grey crosses) as a function of time after gate voltage is switched on at t = 0. The inset shows the ω_R thiophene ring stretch vibration region of FTIR spectra taken before (black) and after (blue) V_G is turned on for 14,000 s.

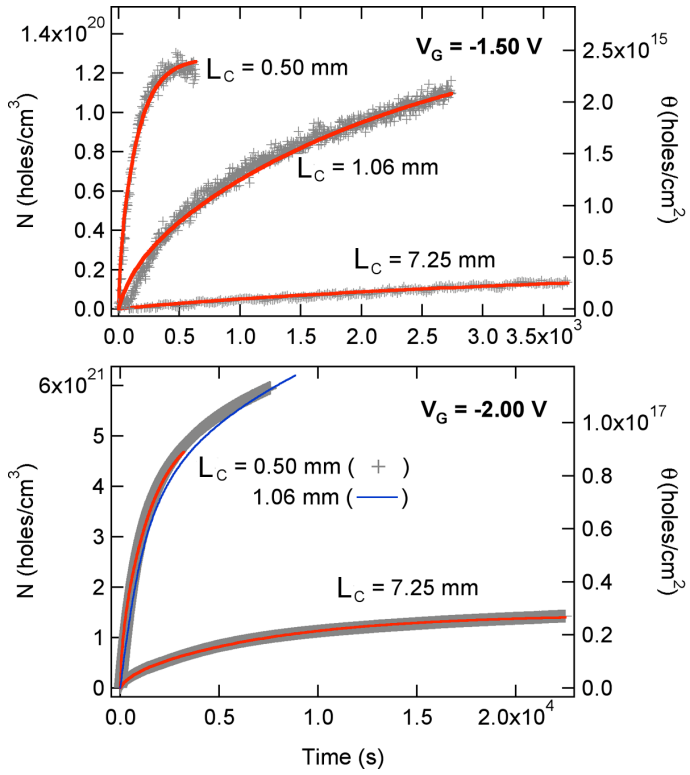

Figure 4.3 Polaron concentration as a function of time after the gate voltage is turned on from $V_G = 0$ to $V_G = -1.5$ V (upper) or -2.0 V (lower) for the three channel lengths indicated ($L_C = 0.50$, 1.06, 7.25 mm). The crosses are data points obtained from the peak area of the polaron transition in FTIR spectra, while the red curves are fits to 1D diffusion models. Note that in the lower panel, for easy distinction from that at $L_C = 0.50$ mm, the polaron uptake for $L_C = 1.06$ mm is shown in blue and its fit is omitted.

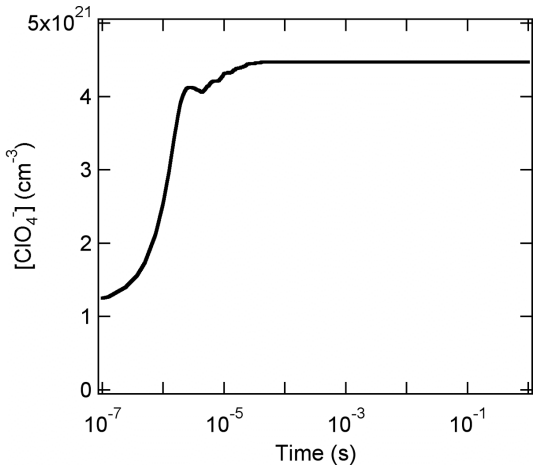

Figure 4.4 Simulated perchlorate ion concentration at the dielectric/semiconductor interface as a function of time. We carried out simulation via the finite element method using the COMSOL Multiphysics package.

4.5 References

[1] F. M. Gray, Solid Polymer Electrolytes: Fundamentals and Technological Applications **1991** (VCH New York).

[2] J. Takeya, K. Yamada, K. Hara, K. Shigeto, K. Tsukagoshi, S. Ikehata, Y. Aoyagi, *Appl. Phys. Lett.* **2006**, 88, 112102.

[3] M. J. Panzer, C. D. Frisbie, *Appl. Phys. Lett.* **2006**, 88, 203504.

[4] M. J.Panzer, C. R. Newman, C. D. Frisbie, *Appl. Phys. Lett.* **2005,** 86, 103503.

[5] M. J. Panzer, C. D. Frisbie, *J. Am. Chem. Soc.* **2007**, 129, 6599.

[6] A. S. Dhoot, J. D. Yuen, M. Heeney, I. McCulloch, D. Moses, A. J. Heeger, *Proc. Nat. Acad. Sci. USA* **2006**, 103, 11834.

[7] L. G. Kaake, Y. Zou, M. J. Panzer, C. D. Frisbie, X-Y. Zhu, *J. Am. Chem. Soc*. **2007**, 129, 7824.

[8] J. D. Yuen, A. S. Dhoot, E. B. Namdas, N. E. Coates, M. Heeney, I. McCulloch, D. Moses, A. J. Heeger, *J. Am. Chem. Soc.* **2007**, 129**,** 14367.

[9] L. Kaake, X.-Y. Zhu, *J. Phys. Chem. C* **2008**, 112, 16174.

[10] P. J. Brown, H. Sirringhaus, M. Harrison, M. Shkunov, R. H. Friend, *Phys. Rev. B*. **2001**, 63, 125204.

[11] R. Osterbacka, C. P. An, X. M. Jiang, Z. V. Vardeny, *Science*, **2000**, 287, 839.

[12] Z. Q. Li, G. M.Wang, N. Sai, D. Moses, M. C. Martin, M. Di Ventra, A.J. Heeger, D. N. Basov, *Nano Lett.* **2006**, 6, 224.

[13] B. Horovitz, R. Osterbaka, Z. V. Vardeny, *Synth. Met.* **2004**, 141, 179.

[14] M. M. Erwin, J. McBride, A. V. Kadavanich, S. J. Rosenthal, *Thin Solid Films* **2002**, 409, 198.

[15] S.-I. Kuroda, K. Marumoto, T. Sakanaka, N. Takeuchi, Y. Shimoi, S. Abe, H. Kokubo, T. Yamamoto, *Chem. Phys. Lett.* **2007**, 435, 273.

[16] K. Tashiro, K. Ono, Y. Minagawa, M. Kobayashi, T. Kawai, K. Yoshino, J. Poly. Sci. B: Poly. Phys. **2003**, 29, 1223.

[17] Q. Pei, G. Yu, C. Zhang, Y. Yang, A. J. Heeger, Science **1995**, 269, 1086.

[18] D. L. Powers, *Boundary Value Problems*, 3rd Ed. **1987** (Harcourt Brace College Publishers, Fort Worth).

[19] K. Kaneto, H. Agawa, K. Yoshino, *J. Appl. Phys.* **1987**, 61, 1197.

[20] K. West, M. A. Careem, S. Skaarup, *Solid State Ionics*, **1990**, 60, 153.

[21] M. J. González-Tejera, E. Sánchez de la Blanca, I Carrillo, M. I. Redondo, M. A. Raso, J. Tortajada, M. V. García, *Synth. Met.* **2005**, 151, 100.

[22] H. Shimotani, G. Diguet, Y. Iwasa, *Appl. Phys. Lett*. **2005**, 86, 022104.

[23] Y. Roichman, N. Tessler, *Appl. Phys. Lett.* **2002**, 80, 1948.

[24] M. Volel, M. Armand, W. Gorecki, *Macromolecules*. **2004**, 37, 8373.

[25] Y. Duan, J.W. Halley, L. Curtiss, P. Redfern, *J. Chem. Phys.* **2005**, 122, 054702.

Chapter 5. Complete Bibliography

5.1 Chapter 1 References

[1] B. A. Bolto, R. McNeill, D. E. Weiss, *Aust. J. Chem.* **1963**, 19, 1090.

[2] R. McNeill, D. E. Weiss, D. Willis *Aust. J. Chem.* **1965**, 18, 477.

[3] B. A. Bolto, D. E. Weiss, D. Willis *Aust. J. Chem.* **1965**, 18, 487.

[4] J. McGinness, P. Corry, P. Proctor *Science*, **1974**, 183, 853.

[5] H. Shirakawa, E. J. Louis, A. G. MacDiarmid, C. K. Chiang, A. J. Heeger *J. Chem. Soc. Chem. Comm.*, **1977**, 474, 578.

[6] M. C. J. M. Vissenberg, M. Matters *Phys. Rev. B* **1998**, 57, 12964.

[7] D. L. Powers *Boundary Value Problems*, 3rd Ed. **1987** (Harcourt Brace College Publishers, Fort Worth).

[8] S.-S. Sun, N. S. Sariciftci *Organic Photovoltaics: Mechanisms, Materials and Devices* **2005** (CRC Press).

[9] H. Gommans, S. Schols, A. Kadashchuk, P. Heremans, S. C. J. Meskers *J. Phys. Chem. C* **2009**, 113, 2974.

[10] A. Kahn, N. Koch, W. Gao *J. Polymer Science B: Polymer Phys.* **2003**, 41, 2529.

[11] D. Cahen, A. Kahn *Adv. Mater.* **2003**, 15, 271.

[12] W. R. Salaneck, R. H. Friend, J. L. Bredas *Phys. Rep.* **1999**, 319, 231.

[13] N. Koch *J. Phys. Condens. Matter* **2008**, 20, 184008.

[14] F. Flores, C. Tejedor *J. Phys. Chem. C* **1987**, 20, 145.

[15] W. Mönch *Surf. Sci.* **1994**, 299, 928.

[16] H. Vázquez, R. Oszwaldowski, P. Pou, J. Ortega, R. Perez, F. Flores, A. Kahn *Europhys. Lett.* **2004**, 65, 802.

[17] H. Vázquez, F. Flores, R. Oszwaldowski, J. Ortega, R. Perez, A. Kahn *Appl. Surf. Sci.* **2004**, 234, 107.

[18] H. Vázquez, W. Gao, F. Flores, A. Kahn *Phys. Rev. B* **2005**, 71, 041306.

[19] A. Kahn, W. Zhao, W. Gao, H. Vázquez, F. Flores *Chem. Phys.* **2006**, 325, 129.

[20] C. Tengstedt, W. Osikowwicz, W. R. Salaneck, I. D. Parker, Che-H. Hsu, M. Fahlman *Appl. Phys. Lett.* **2006**, 88, 053502.

[21] S. Braun, W. Osikowicz, Y. Wang, W. R. Salaneck *Org. Electron.* **2007**, 8, 14.

[22] A. Crispin, X. Crispin, M. Fahlman, M. Berggren, W. R. Salaneck *Appl. Phys. Lett.* **2006**, 89, 213503.

[23] G. Dennler, M. C. Scharber, T. Ameri, P. Denk, K. Forberich, C. Waldauf, C. J. Brabec *Adv. Mater.* **2008**, 20, 579.

[24] J. Hwang, A. Wan, A. Kahn *Mater. Science Eng. R* **2009**, 64, 1.

[25] J. Y. Kim, S. H. Kim, H.-H. Lee, K. Lee, W. Ma, X. Gong, A. J. Heeger, *Adv. Mat.* **2006**, 18, 572.

[26] G. Li, V. Shrotriya, J, Huang, Y. Yao, T. Moriarty, K. Emery, Y. Yang, *Nat. Mater.* **2005**, 4, 864.

[27] Y. Kim, S. Cook, S. M. Tuladhar, S. A. Choulis, J. Nelson, J. R. Durrant, D. D. C. Bradley, M. Giles, I. McCulloch, C.-S. Ha, M. Ree, *Nat. Mater.* **2006**, 5, 197.

[28] W. Osikowicz, M. P. de Jong, W. R. Salaneck, *Adv. Mater.* **2007**, 19, 4213.

[29] V. I. Arkipov, H. Bässler, *Phys. Status Solidi A* **2004**, 201, 1152.

[30] G. Yu, J. Gao, J. Hummelen, F. Wudl, A. J. Heeger *Science* **1995**, 270, 1789.

[31] J. J. M. Halls, C. A. Walsh, N. C. Greenham, E. A. Marseglia, R. H. Friend, S. C. Moratti, A. B. Holmes *Nature* **1995**, 376, 498.

[32] F. Yang, M. Shtein, S. R. Forrest *Nat. Mater.* **2005**, 4, 37.

[33] N. S. Sariciftci, L. Smilowitz, A. J. Heeger, F. Wudl *Science* **1992**, 258, 1474.

[34] J. Y. Kim, K. Lee, N. E. Coates, D. Moses, T.-Q. Nguyen, M. Dante, A. J. Heeger *Science* **2007**, 317, 222.

[35] W. Ma, C. Yang, X. Gong, K. Lee, A. J. Heeger *Adv. Funct. Mater.* **2005**, 15, 1617.

[36] S. H. Park, A. Roy, S. Beaupré, S. Cho, N. Coates, J. S. Moon, D. Moses, M. Leclerc, K. Lee, A. J. Heeger *Nature Photon.* **2009**, 3, 297.

[37] V. D. Mihailetchi, L. J. A. Koster, J. C. Hummelen, P. W. M. Blom, *Phys. Rev. Lett.* **2004**, 93, 216601.

[38] I. Riedel, J. Parisi, V. Dyakonov, L. Lutsen, D. Vanderzande, J. C. Hummelen *Adv. Funct. Mater.* **2004**, 14, 38.

[39] P. Schilinsky, C. Waldauf, C. J. Brabec *Appl. Phys. Lett.* **2002**, 81, 3885.

[40] V. I. Arkhipov, P. Heremans, H. Bässler, *Appl*. *Phys*. *Lett*. **2003**, 82, 4605.

[41] R. A. Marsh, C. R. McNeill, A. Abrusci, A. R. Campbell, R. H. Friend, *Nano Lett.* **2008**, 8, 1393.

[42] H. Ohkita, S. Cook, Y. Astuti, W. Duffy, S. Tierney, W. Zhang, M. Heeney, I. McCulloch, J. Nelson, D. D. C. Bradley, J. R. Durrant, *J. Am. Chem. Soc.* **2008**, 130, 3030.

[43] P. Peumans, A. Yakimov, S. R. Forrest *J. Appl. Phys.* **2003**, 93, 3693.

[44] M. C. Scharber, D. Mühlbacher, M. Koppe, P. Denk, C. Waldauf, A. J. Heeger, and C. J. Brabec *Adv. Mater.* **2006**, 18, 789.

[45] L. J. A. Koster, V. D. Mihailetchi, P. W. M. Blom *Appl. Phys. Lett.* **2006**, 88, 093511.

[46] E. Bundgaard, F. C. Krebs *Sol. En. Mater. Sol. Cells* **2007**, 91, 954.

[47] G. Horowitz *Adv. Mater.* **1998**, 10, 365.

[48] C. D. Dimitrakapoulos, P. R. L. Malenfant *Adv. Mater.* **2002**, 14, 99.

[49] A. R. Brown, C. P. Jarrett, D. M. de Leeuw, M. Matters *Synth. Met.* **1997**, 88, 37.

[50] M.-H. Yoon, A. Facchetti, T. J. Marks *Proc. Nat. Acad. Sci.* USA **2005**, 102, 4678.

[51] S. Ju, K. Lee, D. B. Janes, M.-H. Yoon, A. Facchetti, T. J. Marks *Nano Lett.* **2005**, 5, 2281.

[52] S. Ju, D. B. Janes, G. Lu, A. Facchetti, T. J. Marks *Appl. Phys. Lett.* **2006**, 89, 193506.

[53] J. Lee, M. J. Panzer, Y. He, T. P. Lodge, C. D. Frisbie *J. Am. Chem. Soc.* **2007**, 129, 4532.

[54] F. M. Gray, *Solid Polymer Electrolytes: Fundamentals and Technological Applications* **1991** (VCH, New York).

[55] J. Takeya, K. Yamada, K. Hara, K. Shigeto, K. Tsukagoshi, S. Ikehata, Y. Aoyagi *Appl. Phys. Lett.* **2006**, 88**,** 112102.

[56] M. J. Panzer, C. D. Frisbie *Appl. Phys. Lett.* **2006**, 88, 203504.

[57] M. J.Panzer, C. R. Newman, C. D. Frisbie, *Appl. Phys. Lett.* **2005**, 86, 103503.

[58] M. J. Panzer, C. D. Frisbie, *J. Am. Chem. Soc.* **2007**, 129, 6599.

[59] A. S. Dhoot, J. D. Yuen, M. Heeney, I. McCulloch, D. Moses, A. J. Heeger, *Proc. Nat. Acad. Sci. USA* **2006**, 103, 11834.

[60] L. G. Kaake, Y. Zou, M. J. Panzer, C. D. Frisbie, X-Y. Zhu, *J. Am. Chem. Soc*. **2007**, 129, 7824.

[61] J. D. Yuen, A. S. Dhoot, E. B. Namdas, N. E. Coates, M. Heeney, I. McCulloch, D. Moses, A. J. Heeger, *J. Am. Chem. Soc.* **2007**, 129, 14367.

5.2 Chapter 2 References

[1] J. E. Stewart *Infrared Spectroscopy Experimental Methods and Techniques* **1970** (Marcel Dekker Inc., New York).

[2] Y. Jun, X.-Y. Zhu *J. Am. Chem. Soc.* **2004**, 126, 13224.

[3] A. Chattopadhyay, S. G. Boxer *J. Am. Chem. Soc.* **1995**, 117, 1449.

[4] L. N. Silverman, M. E. Pitzer, P. O. Ankomah, S. G. Boxer, E. E. Fenlon *J. Phys. Chem. B Lett.* **2007**, 111, 11611.

[5] L. W. Barbour, R. D. Pensack, M. Hegadorn, S. Arzhantsev, J. B. Asbury *J. Phys. Chem. C* **2008**, 112, 3926.

[6] R. D. Pensack, K. M. Banyas, L. W. Barbour, M. Hegadorn, J. B. Asbury *Phys. Chem. Chem. Phys.* **2009**, 11, 2575.

5.3 Chapter 3 References

[1] M. C. Scharber, D. Mühlbacher, M. Koppe, P. Denk, C. Waldauf, A. J. Heeger, C. J. Brabec *Adv. Mater.* **2006**, 18, 789.

[2] J. Xue, S. Uchida, B. P. Rand, S. R. Forrest *Appl. Phys. Lett.* **2004**, 85, 5757.

[3] V. I. Arkipov, H. Bässler *Phys. Status Solidi A* **2004**, 201, 1152.

[4] J. Y. Kim, S. H. Kim, H.-H. Lee, K. Lee, W. Ma, X. Gong, A. J. Heeger *Adv. Mat.* **2006**, 18, 572.

[5] G. Li, V. Shrotriya, J, Huang, Y. Yao, T. Moriarty, K. Emery, Y. Yang *Nat. Mater.* **2005**, 4, 864.

[6] Y. Kim, S. Cook, S. M. Tuladhar, S. A. Choulis, J. Nelson, J. R. Durrant, D. D. C. Bradley, M. Giles, I. McCulloch, C.-S. Ha, M. Ree *Nat. Mater.* **2006**, 5, 197.

[7] W. Osikowicz, M. P. de Jong, W. R. Salaneck *Adv*. *Mater*. **2007**, 19, 4213.

[8] V. I. Arkhipov, P. Heremans, H. Bäsler *Appl*. *Phys*. *Lett*. **2003**, 82, 4605.

[9] R. A. Marsh, C. R. McNeill, A. Abrusci, A. R. Campbell, R. H. Friend *Nano Lett.* **2008**, 8, 1393.

[10] H. Ohkita, S. Cook, Y. Astuti, W. Duffy, S. Tierney, W. Zhang, M. Heeney, I. McCulloch, J. Nelson, D. D. C. Bradley, J. R. Durrant *J. Am. Chem. Soc.* **2008**, 130, 3030.

[11] D. K. Lambert *Solid State Commun.* **1984**, 51, 297.

[12] A. Chattopadhyay, S. G. Boxer *J. Am. Chem. Soc.* **1995**, 117, 1449.

[13] L. N. Silverman, M. E. Pitzer, P. O. Ankomah, S. G. Boxer, E. E. Fenlon *J. Phys. Chem. B Lett.* **2007**, 111, 11611.

[14] R. D. Pensack, K. M. Banyas, L. W. Barbour, M. Hegadorn, J. B. Asbury *Phys. Chem. Chem. Phys.* **2009**, 11, 2575.

[15] L. W. Barbour, R. D. Pensack, M. Hegadorn, S. Arzhantsev, J. B. Asbury, *J. Phys. Chem. C* **2008**, 112, 3926.

[16] E. S. Park, S. G. Boxer *J. Phys. Chem. B* **2002**, 106, 5800.

[17] W. Ma, C. Yang, X. Gong, K. Lee, A. J. Heeger *Adv. Funct. Mater.* **2005**, 15, 1617.

[18] P. Schilinsky, U. Asawapirom, U. Scherf, M. Biele, C. J. Brabec *Chem. Mater.* **2005**, 17, 2175.

[19] X. Yang, J. Loos, S. C. Veenstra, W. J. H. Verhees, M. M. Wienk, J. M. Kroon, M. A. J. Michels, R. A. J. Janssen *Nano Lett.* **2005**, 5, 579.

[20] T. A. Bull, L. S. C. Pingree, S. A. Jenekhe, D. S. Ginger, C. K. Luscombe *ACS Nano*, **2009**, 3, 627.

[21] S. Nilsson, A. Bernasik, A. Budkowski, E. Moons *Macromolecules*, **2007**, 40, 8291.

[22] M. Campoy-Quiles, T. Ferenczi, T. Agostinelli, P. G. Etchegoin, Y. Kim, T. D. Anthopoulos, P. N. Stavrinou, D. D. C. Bradley, J. Nelson *Nat. Mater.* **2008**, 7, 158.

[23] G. Dennler, M. C. Scharber, C. J. Brabec *Adv. Mater.* **2009**, 21, 1.

[24] A. M. Ballantyne, L. Chen, J. Dane, T. Hammant, F. M. Braun, M. Heeney, W. Duffy, I. McCulloch, D. D. C. Bradley, J. Nelson *Adv. Funct. Mater*. **2008**, 18, 2373.

[25] R. C. Hiorns, R. de Bettignies, J. Leroy, S. Bailly, M. Firon, C. Sentein, A. Khoukh, H. Preud'homme, C. Dagron-Lartigau *Adv. Funct. Mater.* **2006**, 16, 2263.

[26] R. U. A. Kahn, D. Poplavskyy, T. Kreouzis, D. D. C. Bradley *Phys. Rev. B* **2007**, 75, 035215.

[27] Q. Shi, Y. Hou, J. Lu, H. Jin, Y. Li, Y. Li, X. Sun, J. Liu *Chem. Phys. Lett.* **2006**, 425, 353.

[28] K. Hummer, P. Puschnig, S. Sagmeister, C. Ambrosch-Draxl *Mod. Phys. Lett. B* **2006**, 20, 261.

[29] W. Ma, J. Y. Kim, K. Lee, A. J. Heeger *Macromol. Rapid Commun.* **2007**, 28, 1776.

[30] H. Vázquez, R. Oszwaldowski, P. Pou, J. Ortega, R. Perez, F. Flores, A. Kahn *Europhys. Lett.* **2004**, 65, 802.

[31] H. Vázquez, F. Flores, R. Oszwaldowski, J. Ortega, R. Perez, A. Kahn *Appl. Surf. Sci.* **2004**, 234, 107.

[32] H. Vázquez, W. Gao, F. Flores, A. Kahn *Phys. Rev. B* **2005**, 71, 041306.

[33] A. Kahn, W. Zhao, W. Gao, H. Vázquez, F. Flores *Chem. Phys.* **2006**, 325, 129.

[34] C. Tengstedt, W. Osikowwicz, W. R. Salaneck, I. D. Parker, Che-H. Hsu, M. Fahlman *Appl. Phys. Lett.* **2006**, 88, 053502.

[35] S. Braun, W. Osikowicz, Y. Wang, W. R. Salaneck *Org. Electron.* **2007**, 8, 14.

[36] A. Crispin, X. Crispin, M. Fahlman, M. Berggren, W. R. Salaneck *Appl. Phys. Lett.* **2006**, 89, 213503.

[37] B. Smith *Infrared Spectral Interpretation: A Systematic Approach* **1998** (CRC Press).

[38] H.-L. Cheng, W.-Y. Chou, C.-W. Kuo, Y.-W. Wang, Y.-S. Mai, F.-C. Tang, S.-W. Chu *Adv. Funct. Mater.* **2008**, 18, 285.

[39] F. S. Tautz, S. Sloboshanin, J. A. Schaefer, R. Scholz, V. Shklover, M. Sokolowski, E. Umbach *Phys. Rev. B.* **2000**, 61, 16933.

5.4 Chapter 4 References

[1] F. M. Gray, Solid Polymer Electrolytes: Fundamentals and Technological Applications **1991** (VCH New York).

[2] J. Takeya, K. Yamada, K. Hara, K. Shigeto, K. Tsukagoshi, S. Ikehata, Y. Aoyagi, *Appl. Phys. Lett.* **2006**, 88, 112102.

[3] M. J. Panzer, C. D. Frisbie, *Appl. Phys. Lett.* **2006**, 88, 203504.

[4] M. J.Panzer, C. R. Newman, C. D. Frisbie, *Appl. Phys. Lett.* **2005,** 86, 103503.

[5] M. J. Panzer, C. D. Frisbie, *J. Am. Chem. Soc.* **2007**, 129, 6599.

[6] A. S. Dhoot, J. D. Yuen, M. Heeney, I. McCulloch, D. Moses, A. J. Heeger, *Proc. Nat. Acad. Sci. USA* **2006**, 103, 11834.

[7] L. G. Kaake, Y. Zou, M. J. Panzer, C. D. Frisbie, X-Y. Zhu, *J. Am. Chem. Soc.* **2007**, 129, 7824.

[8] J. D. Yuen, A. S. Dhoot, E. B. Namdas, N. E. Coates, M. Heeney, I. McCulloch, D. Moses, A. J. Heeger, *J. Am. Chem. Soc.* **2007**, 129**,** 14367.

[9] L. Kaake, X.-Y. Zhu, *J. Phys. Chem. C* **2008**, 112, 16174.

[10] P. J. Brown, H. Sirringhaus, M. Harrison, M. Shkunov, R. H. Friend, *Phys. Rev. B.* **2001**, 63, 125204.

[11] R. Osterbacka, C. P. An, X. M. Jiang, Z. V. Vardeny, *Science*, **2000**, 287, 839.

[12] Z. Q. Li, G. M.Wang, N. Sai, D. Moses, M. C. Martin, M. Di Ventra, A.J. Heeger, D. N. Basov, *Nano Lett.* **2006**, 6, 224.

[13] B. Horovitz, R. Osterbaka, Z. V. Vardeny, *Synth. Met.* **2004**, 141, 179.

[14] M. M. Erwin, J. McBride, A. V. Kadavanich, S. J. Rosenthal, *Thin Solid Films* **2002**, 409, 198.

[15] S.-I. Kuroda, K. Marumoto, T. Sakanaka, N. Takeuchi, Y. Shimoi, S. Abe, H. Kokubo, T. Yamamoto, *Chem. Phys. Lett.* **2007**, 435, 273.

[16] K. Tashiro, K. Ono, Y. Minagawa, M. Kobayashi, T. Kawai, K. Yoshino, J. Poly. Sci. B: Poly. Phys. **2003**, 29, 1223.

[17] Q. Pei, G. Yu, C. Zhang, Y. Yang, A. J. Heeger, Science **1995**, 269, 1086.

[18] D. L. Powers, *Boundary Value Problems*, 3rd Ed. **1987** (Harcourt Brace College Publishers, Fort Worth).

[19] K. Kaneto, H. Agawa, K. Yoshino, *J. Appl. Phys.* **1987**, 61, 1197.

[20] K. West, M. A. Careem, S. Skaarup, *Solid State Ionics*, **1990**, 60, 153.

[21] M. J. González-Tejera, E. Sánchez de la Blanca, I Carrillo, M. I. Redondo, M. A. Raso, J. Tortajada, M. V. García, *Synth. Met.* **2005**, 151, 100.

[22] H. Shimotani, G. Diguet, Y. Iwasa, *Appl. Phys. Lett*. **2005**, 86, 022104.

[23] Y. Roichman, N. Tessler, *Appl. Phys. Lett.* **2002**, 80, 1948.

[24] M. Volel, M. Armand, W. Gorecki, *Macromolecules*. **2004**, 37, 8373.

[25] Y. Duan, J.W. Halley, L. Curtiss, P. Redfern, *J. Chem. Phys.* **2005**, 122, 054702.